TRENT2D*: An accurate numerical approach to the simulation of two-dimensional dense snow avalanches in global coordinate systems

Daniel Zugliani *, Giorgio Rosatti

Department of Civil, Environmental and Mechanical Engineering, University of Trento, Italy

ARTICLE INFO

ABSTRACT

The paper presents a novel and accurate numerical approach to the simulation of two-dimensional, dense snow avalanches described as a single-phase, shallow fluids with a Voellmy friction law.

Unlike the majority of the shallow-flow models present in the literature, using a local coordinate system (one axis normal to the bed and the other two lying in the tangent plane), our approach considers a global three-dimensional Cartesian coordinate system with an axis opposite to the gravity vector and the other two lying in a horizontal plane. The relevant flow equations, accounting for significant bed slope, have been derived in conservative form for the 1D and 2D cases. This choice allows overcoming an intrinsic limit of the local approach that ceases to be valid in case of vertical walls.

From a numerical point of view, the model employs a finite volume scheme applied to a regular Cartesian grid where the fluxes are evaluated with a well-balanced Godunov method. The source term is computed with an implicit operator-splitting technique tailored to deal not only with dynamic conditions but also with stopping conditions due to the Coulomb-type term in the Voellmy friction law. Finally, an effective numerical strategy was developed to treat static conditions with an inclined free surface.

Several tests, some with analytical solution and some without, were performed to evaluate the capabilities of the proposed approach. Results are satisfactory: all the analytical solutions are accurately reproduced while the other tests give reliable results. Finally, no instability arises in any situation. For these reasons, TRENT2D* is a candidate to become a good model also for practical applications such as hazard mapping and hazard assessments.

1. Introduction

Since Voellmy's early work (Voellmy, 1955), the mathematical modelling of dense snow avalanches is commonly based on a continuum fluid approach with non-Newtonian rheology. The shallowness of the flow along the normal to the bed and the relevant depth-averaged variables are also commonly employed. The flow problem is then described by a system of partial differential equations deriving from the mass and momentum balance. Models differ essentially in the assumptions concerning the velocity profile, the friction law and the normal stress distribution along sections normal to the flow direction (for an overview, see e.g., Bartelt et al., 1999; Barbolini et al., 2000; Eglit et al., 2020, and references therein). This description is used for modelling not only snow avalanches but other geophysical flows such as granular flows over fixed bed (e.g., O'Brien et al., 1993; Gray et al., 1999; Pitman and Le, 2005). Finally, other aspects, as the effect of the curvature of the bed and the

frontal and bed entrainment, are subject of active research (e.g., Grigorian and Ostroumov, 2020; Issler, 2020; Peruzzetto et al., 2020).

The pure 1D versions of these models are derived for a constant bed slope and they share the same reference system, composed of an axis normal to the bed and one parallel to it, and pointing in the flow direction. The reason for this choice is that this coordinate system is the simplest to describe these flows where the slope of the bed, with respect to a horizontal direction, can be large. This approach has also been applied to cases in which the bed has small curvatures. In these cases, the coordinate system is defined locally and is composed of two axes respectively normal and tangent to the bed at each point. This viewpoint is commonly called the Local Coordinate System (LCS). Thanks to the assumption of small curvature, the equation system obtained in the pure 1D case can be applied straightforwardly to this more general case. In 2D cases, the majority of the high-slope models (both concerning dense snow avalanches and other flows) share the LCS approach where one

axis is normal to the local bed, while the other two axes lie in the tangent plane. The direction of these two axes can be chosen in different ways leading to different, but substantially equivalent, coordinate systems (see e.g., Iverson and Denlinger, 2001; Bouchut et al., 2003; Mangeney-Castelnau et al., 2003; Bouchut and Westdickenberg, 2004, among others).

Even if it is the most natural, at least in the 1D case, the LCS approach presents an intrinsic limit emerging when the bed becomes vertical and the flow is not aligned with the steepest slope direction (e.g., in case of a side wall). In this case, the flow depth cannot be defined along the normal direction (this being horizontal) and the related system of equations ceases to be valid. Moreover, even when the bed is almost vertical and the flow is not directed along the steepest slope direction, numerical problems can be expected. The vertical or near-vertical bed condition is not something rarely encountered in practical situations: bed discontinuities, natural channels or man-made defense structures with steep walls are only some cases. Therefore, suitable modelling able to deal also with these situations is desirable.

The goal we set for this work was to derive a numerical approach for the description of dense snow avalanches that was accurate in any practical situation. As a reference model, we chose the Voellmy-fluid approach (Salm, 1993) without longitudinal straining, since it is simple, widely applied and its main features are shared by several other models.

To reach the target, we started from the know-how developed for the TRENT2D model (Armanini et al., 2009). For the description of the flow, we used a three-dimensional, Cartesian Global Coordinate System (GCS), consisting of a vertical ascending axis (i.e. opposite to the gravity vector) and two orthogonal axes lying, arbitrarily oriented, in the horizontal plane. This viewpoint is commonly employed in Shallow Water (SW) models for rivers, where the direction normal to the bed can be approximated to the vertical direction, but is rarely used when the bed is steep. Some examples of GCS approaches can be found in Vreugdenhil (1994); Gerbeau and Perthame (2001); Mangeney et al. (2007) and, more recently in Juez et al. (2013), where the authors compared numerically the LCS and GCS approaches applied to homogeneous fluid flows with pure Coulomb bed shear stresses. Nevertheless, to the best of our knowledge, nobody used this approach for snow avalanches. For this reason, and the sake of completeness, in this paper, we present the complete derivation of the Voellmy-fluid model equations in a GCS for the pure 1D case and then we extend the derivation to the 2D case. This last system is similar to the classical SW system but with some particular elements deriving from the condition of non-negligible bed slope. Following Rosatti and Begnudelli (2010), the introduction of the bed level as a field variable and the addition of the equation for its time invariance allows dealing also with bed discontinuities.

As for the numerical approach, we used the basic strategy used in TRENT2D, namely a finite volume scheme on a regular Cartesian grid with fluxes evaluated with a well-balanced Godunov method and an implicit operator splitting for the evaluation of the source term. This last technique has here been adapted to deal with all the cases involving no-motion conditions due to the Coulomb-type term present in the Voellmy friction law, namely starting and stopping of the flow and maintenance of static conditions with inclined free surface. The quality of the new model, called TRENT2D[*] (pronounced *TRENT2D snowflake*), was assessed by comparing the numerical results with some analytical solutions and with the results of the RAMMS::AVALANCHE code (Christen et al., 2008, 2010).

The paper is structured as follows. In Section 2, the assumptions of the model are reported in detail. In Section 3, the pure 1D depth-averaged mass and momentum balance equation system is derived in a GCS while the extension to the 2D case is presented in Section 4. The numerical method is described in Section 5 while test cases are presented and discussed in Section 6. Conclusions end the paper.

2. Model assumptions

As we said in the Introduction, the reference model we use in this work is the Voellmy-fluid model without longitudinal straining. For sake of completeness, in Section 2.1 we recall the general assumptions that will be used in the derivation of the GCS formulation and that are shared with many other published models. In Section 2.2 we recall the specific assumptions for the Voellmy-fluid model that distinguish this approach from other models described in the literature.

2.1. General assumptions

1. An avalanche can be treated as a continuous, homogeneous fluid whose motion can be described by a suitable system of partial differential equations deriving from mass and momentum balance (Salm, 1993).
2. The density ρ is constant in time and space (e.g., the dense layer in Sampl and Zwinger, 2004).
3. The flow occurs on a fixed bed with a potentially steep slope with respect to a horizontal reference plane. Therefore, the assumption that the normal to the bed can be approximated with the vertical direction (assumption commonly employed in de Saint-Venant equations for rivers) is not valid in this context.
4. Called ε the ratio between the snow depth (measured in the direction normal to the bed) and a characteristic planar dimensions of a snow avalanche, field evidences (Butler and Malanson, 1985; Sovilla et al., 2006) show that $\varepsilon \ll 1$. This condition, commonly called Shallow Flow (SF) condition, allows to neglect all the terms in the momentum balances that, by applying a scale analysis, appear to be $O(\varepsilon)$. These are the inertial terms and the shear stresses in the momentum balance along the normal direction and the transverse shear stresses in the momentum balances along two orthogonal direction laying in a plane parallel to the plane tangent to the bed (Savage and Hutter, 1989; Gray et al., 1999; Iverson and Denlinger, 2001). The consequences are:
   - the velocity in the normal direction is negligible and any velocity vector lies on a plane parallel (or locally tangent) to the bed;
   - the piezometric head $p + \rho g z$ is constant along a direction normal to the bed, where p is the pressure, g is the modulus of the gravity vector $\overrightarrow{g}$ and z is an elevation measured in the upward vertical direction (opposite to the gravity vector $\overrightarrow{g}$) above a reference horizontal plane; in other words, the pressure distribution is "hydrostatic" normally to the bed;
   - the flow can be adequately described by using depth-averaged quantities.
5. The curvature of the bed is negligible. Therefore:
   - the equations derived for the constant slope case can be applied locally referring to the tangent plane;
   - the pressure distribution along the local normal to the bed is hydrostatic, i.e., it is not affected by curvature effects (e.g., Mangeney et al., 2007).
6. Normal and shear stresses on the free surface are negligible (e.g., Mangeney et al., 2007).

2.2. Voellmy-fluid assumptions

1. The velocity distribution is constant along the direction normal to the bed. Therefore, the point velocity $\overrightarrow{U}'$ along the normal direction and the depth-averaged velocity $\overrightarrow{U}$ have the same norm. We will conventionally locate this last vector in the middle of the depth.
2. According to Bartelt et al. (1999), active-passive longitudinal straining has little influence on the flow calculation. Therefore, this feature has been neglected compared to the original Voellmy-fluid model.
3. As for the bed shear stress vector, we write it in the following way:

$$\overrightarrow{\tau}_0 = -\tau_0 \widehat{s}^\tau \tag{1}$$

where τ_0 is the norm of the vector and $\widehat{s}^\tau$ is a unit vector pointing in the opposite direction to the bed shear stress vector. According to the Voellmy-fluid approach, we must distinguish the following two cases.

Static case: no additional expression is required for $\overrightarrow{\tau}_0$ since it can be computed directly from the momentum balances with null velocities. A detailed expression of this vector will be provided in Section 3.6 for the 1D case, and in Section 4.2 for the 2D case. The static condition occurs up to values of τ_0 equal to a Coulomb-type threshold value expressed by:

$$\tau_c = p_b \mu \tag{2}$$

where p_b is the pressure at the bed level and μ is the dimensionless Coulomb friction coefficient.

Dynamic case: in this case $\tau_0 = \tau_v$, where

$$\tau_v = \tau_c + \frac{\rho g}{\xi} \left\| \overrightarrow{U} \right\|^2 \tag{3}$$

is the Voellmy friction law in which ξ is a suitable friction coefficient. As for the direction, the bed shear stress vector is assumed to be aligned and opposite to the depth-averaged velocity vector. Therefore, we can write:

$$\widehat{s}^\tau = \frac{\overrightarrow{U}}{\left\| \overrightarrow{U} \right\|} \tag{4}$$

3. Flow equations in the Global Coordinate System - 1D case

In this section we derive the flow equations in the GCS for the 1D case. In particular, we provide the geometrical framework used to describe the flow and the details of the procedure employed in the derivation.

3.1. Geometrical framework

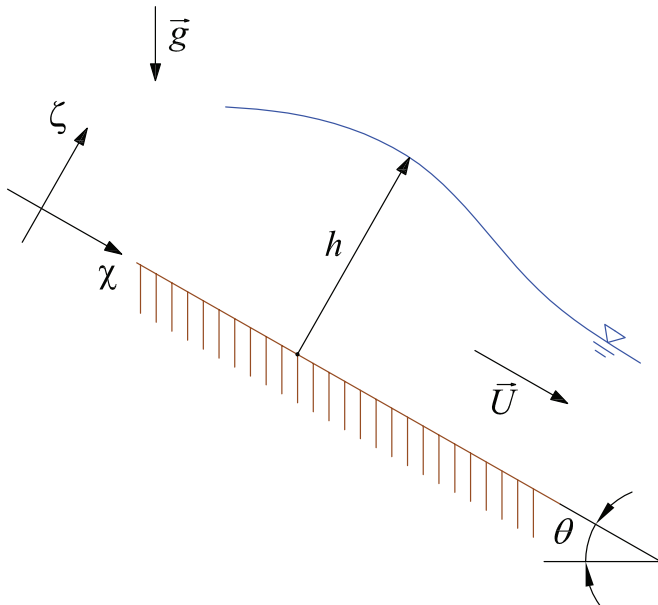Let us consider a slice of an avalanche of unit depth that moves down an inclined plane as in Fig. 1. According to the model assumptions, this flow can be described by using two field variables, namely the flow depth h, measured along the normal direction, and the depth-averaged velocity $\overrightarrow{U}$, conventionally located at the middle of the depth. These variables change in time and, spatially, only in the downslope direction. Therefore, this flow is a pure 1D flow.

The more natural coordinate system for this type of flow is the LCS, here characterized by an axis ζ normal to the bed and the axis χ parallel to the bed and pointing in the downward direction (see Fig. 1). With respect to this system, the field variables can be written as:

$$\overrightarrow{U}(\chi, h(\chi)/2, t) = (U_\chi(\chi, t), 0) \tag{5}$$

$$\overrightarrow{h}(\chi, 0, t) = (h(\chi, t), 0) \tag{6}$$

Therefore, we have two independent (χ and t) and two dependent (U_χ and h) variables. The equations that define this flow problem are the differential mass balance equation and the differential χ-momentum balance equation along the χ direction. Hydrostatic distribution of the pressure along ζ and the Voellmy relations for the bed shear stress close the problem.

Let us consider now a GCS composed of a vertical z-axis, with direction opposite to the gravity vector $\overrightarrow{g}$, and a horizontal x-axis, as in Fig. 2. We denote by θ the angle that the inclined plane forms with the x-axis while the unit vectors normal and tangential to the plane are:

$$\widehat{n} = (sin\theta, cos\theta) \tag{7}$$

$$\widehat{t} = (cos\theta, -sin\theta) \tag{8}$$

respectively. Even though the flow is purely 1D, in the GCS the field variables are vectors of two components that change in both the axes directions that generically can be written as:

$$\overrightarrow{U}(x, z, t) = (U_x(x, z, t), U_z(x, z, t))$$

$$\overrightarrow{h}(x, z, t) = (h_x(x, z, t), h_z(x, z, t))$$

Therefore, in this case, we have three independent and four dependent variables. Nevertheless, also the number of equations available for describing the flow increases accordingly. The following observations can be made.
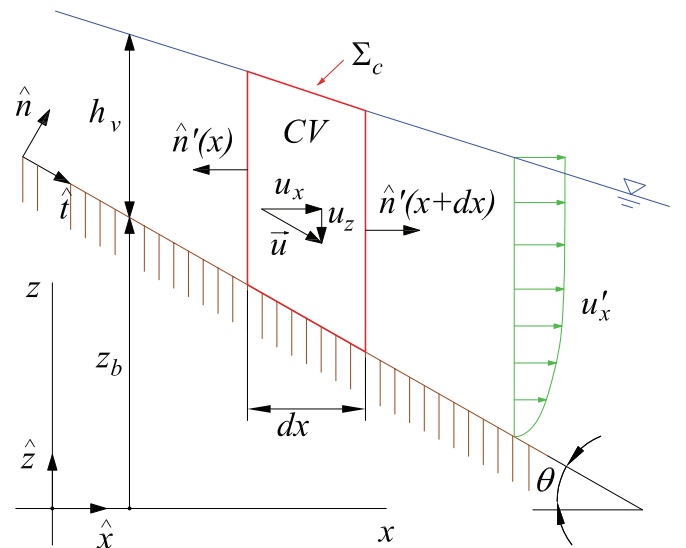

Fig. 1. Pure 1D flow problem described by using a Local Coordinate System.

Fig. 2. Geometry of the infinitesimal Control Volume used for the expression of the Reynolds theorem in CGS and related field variables.

1. The normal depth vector is defined along the the inclined plane. Therefore, the z-coordinate is connected to the x-coordinate via the bed plane equation:

$$z = z_0 - x\tan\theta \tag{9}$$

where z_0 is the bed elevation evaluated at the origin of the x-axis. A similar reasoning can be made considering the depth-averaged velocity vector so we can conclude that z is not an independent variable of the flow problem.

2. The SF assumption gives a constraint on the velocity components that is similar to the previous relation:

$$\frac{U_z}{U_x} = -\tan\theta \tag{10}$$

Therefore, one velocity component is an explicit function of the other component.

3. Instead of using the avalanche depth h, it is possible to identify, in an unequivocal way, the avalanche free-surface position by using the vertical depth h_v since, as will be shown further on, this quantity appears naturally in the derivation of the equations.

4. As for the velocity, it is possible to introduce the vertical-depth averaged velocity vector $\vec{u} = (u_x, u_z)$ (detailed definition will be given in Section 3.2) where the components satisfy a relation similar to Eq. (10). It is useful to use u_x as principal field variable since also this quantity appears naturally in the derivation of the equations.

Thanks to Eq. (9), the total number of independent variables is reduced to two (t and x) while, thanks to remarks 3 and 4, also the number of dependent variables is reduced to two: the vertical depth h_v and the x-component of the velocity vector, u_x.

The available equations involving the field variables are one differential mass balance and one differential momentum balance in the x-direction. Actually, in the momentum equation, a pressure distribution along the vertical direction appears. As will be shown in Section 3.4, this distribution can be derived by exploiting the SF condition.

After all, the pure 1D problem in GCS is characterized by the same number and type of equations as in the classical LCS but the equations are slightly different. In the following Section, these equations will be derived explicitly.

3.1.1. The infinitesimal Control Volume

The derivation of the 1D flow equations is commonly obtained by depth integration of the two-dimensional (in a vertical plane) Cauchy equations (e.g., Savage and Hutter, 1991; Mangeney-Castelnau et al., 2003, among many). Here we prefer to follow the alternative but equivalent path based on the application of the integral mass and momentum balance to a suitable Control Volume (CV). Even if this approach is less frequently used in the literature (e.g., Gerbeau and Perthame, 2001), we think it is more intuitive since it allows to deal with and to understand the physical features in case of bed steps (e.g., Rosatti and Fraccarollo, 2006) and it seems to be more suited to the context of this work.

Referring to Fig. 2, the CV is enclosed by a control surface Σ_c, composed of four surfaces of unit width in the direction normal to the x-z plane: two vertical sections, spanning from the bed to the mobile free surface, located in fixed, generic positions x and $x + dx$; a fixed surface superimposed on the bed and a mobile surface superimposed on the free surface (i.e. with the same vertical velocity as the latter) both spanning between the two vertical sections.

Because of the infinitesimal distance between the two vertical sections, all the field variables located at $x + dx$ can be expressed with a first-order Taylor expansion starting from x. This implies that all the field variables, including the bed surface, change linearly inside the CV. In the derivation of the equations, we assume that all these variables are positive as x increases.

3.2. The Reynolds transport theorem applied to the infinitesimal CV

The Lagrangian variation of a local and instantaneous field variable $a'(x, z, t)$ integrated over a System Volume (SV), instantaneously coincident with the CV, can be expressed in Eulerian form thanks to the Reynolds transport theorem. Since our CV is a mobile one (at least on a part of Σ_c), the generic expression must be employed:

$$\frac{D}{Dt}\int_{SV} a' \, dV = \overbrace{\frac{d}{dt}\int_{CV} a' \, dV}^{\text{Term I}} + \overbrace{\oint_{\Sigma_c} a' \vec{v'} \cdot \hat{n}' \, d\Sigma_c}^{\text{Term II}} \tag{11}$$

where $\vec{v'}$ is the local relative velocity (a difference between the material velocity of the fluid and the velocity of the surface) and $\hat{n}'$ is the outward-pointing unit normal vector relevant to each surface element $d\Sigma_c$. We can rewrite Term I and Term II accounting for the features of the chosen CV and limiting ourselves to $\mathcal{O}(dx)$ terms.

Term I. The term can be written as:

$$\frac{d}{dt}\int_{z_b(x)}^{z_b(x)+h_v(x,t)} a'(x, z, t) \, dz dx \tag{12}$$

where only the first-order term for the volume and the zeroth-order term for a' must be considered in the integral to obtain an overall $\mathcal{O}(dx)$ expression. Introducing the vertical-depth averaged value of a':

$$a(x, t) = \frac{1}{h_v(x, t)}\int_{z_b(x)}^{z_b(x)+h_v(x,t)} a'(x, z, t) \, dz \tag{13}$$

and considering that the time derivative is taken at a fixed position x (so the time derivative becomes a partial time derivative) the final expression reduces to:

$$\frac{d}{dt}\int_{CV} a' \, dV = \frac{\partial}{\partial t}(ah_v) dx \tag{14}$$

where, unlike previously, we have not indicated explicitly the dependencies of the field variables. From now on, we will maintain this convention except in cases where an explicit indication is advisable.

Term II. This term concerns the relative fluxes across the control surface. These fluxes are null across the free surface and the bottom surface since the respective normal relative velocities are null. The flux across the left vertical section located at x, where $d\Sigma_c = dz$, can be written as

$$F_l(x) = \int_{z_b}^{z_b+h_v} a' \vec{v'} \cdot \hat{n}' \, dz$$

and can be further specified considering that the unit normal vector of this section is $\hat{n}' = (-1, 0)$ and that the relative velocity coincides with the particle velocity because the section is fixed. Therefore, the scalar product becomes $\vec{v'} \cdot \hat{n}' = -u'_x$ and the resulting flux is:

$$F_l(x) = -\int_{z_b}^{z_b+h_v} a' u'_x \, dz \tag{15}$$

We can express this flux as a function of vertical-depth averaged quantities:

$$\frac{1}{h_v}\int_{z_b}^{z_b+h_v} a' u'_x \, dz = \alpha_{au_x} a u_x \tag{16}$$

where

$$u_x = \frac{1}{h_v}\int_{z_b}^{z_b+h_v} u'_x \, dz \tag{17}$$

is the vertical-depth averaged value of u'_x and α_{au_x} is a product profile

factor, necessary to express the average of the product of two variables as a function of the product of the relevant averaged variables. The final expression is, therefore:

$$F_l(x) = -h_v a u_x \alpha_{au_x} \tag{18}$$

Along the right vertical section, the unit normal vector is $\widehat{n}' = (1, 0)$ and therefore the relevant scalar product becomes $\overrightarrow{v} \cdot \widehat{n}' = u'_x$ while the relevant flux is then:

$$F_r(x + dx) = \int_{z_b(x+dx)}^{z_b(x+dx,t)+h_v(x+dx,t)} a' u'_x dz$$

As any other variable, also the value of this flux can be expressed as a first-order Taylor expansion:

$$F_r(x + dx) = F_r(x) + \frac{\partial}{\partial x} F_r(x) dx \tag{19}$$

Finally, considering that $F_r(x) = -F_l(x)$, since the relevant normal unit vectors are opposite, Term II, sum of Eq. (18) and Eq. (19), becomes:

$$\oint_{\Sigma_c} a' \overrightarrow{v} \cdot \widehat{n}' d\Sigma_c = \frac{\partial}{\partial x} (h_v a u_x \alpha_{au_x}) dx \tag{20}$$

Considering Eq. (14) and Eq. (20), the final expression of the Reynolds theorem is:

$$\frac{D}{Dt} \int_{SV} a' dV = \left[\frac{\partial}{\partial t} (a h_v) + \frac{\partial}{\partial x} (h_v a u_x \alpha_{au_x}) \right] dx \tag{21}$$

3.3. Mass balance equation

The mass balance equation, in Lagrangian form, is:

$$\frac{D}{Dt} \int_{SV} \rho \, dV = 0 \tag{22}$$

Here we can use Eq. (21) where we set $a' = \rho$. Moreover, ρ being constant, we get $\alpha_{\rho ux} = 1$. Finally, dividing the equation by $\rho \, dx$, we obtain the desired equation:

$$\frac{\partial h_v}{\partial t} + \frac{\partial}{\partial x} (u_x h_v) = 0 \tag{23}$$

3.4. Pressure distribution along the z-direction

We derive now the pressure distribution along the z-direction since this distribution plays a key role in the x-direction momentum balance equation.

Let us consider a point $\mathscr{P}$ located in (x, z) and let us consider an infinitesimal CV of unit width as sketched in Fig. 3, bounded by a surface parallel to the bed and passing through $\mathscr{P}$, two vertical sections spanning from the free surface to the previous surface and distant dx one from the other, and finally by the free surface enclosed between the vertical surfaces.

Let us consider the unit vector $\widehat{n}$ normal to the bed and the corresponding normal momentum $\rho u'_n$. The Lagrangian expression of the normal momentum balance along the normal direction is:

$$\frac{D}{Dt} \int_{SV} \rho u'_n dV = \sum_i F_n^i \tag{24}$$

where F_n^i represents the normal component of the i-th external force acting on the CV.

Considering that the normal velocity is negligible because of the shallow flow assumption, we get that the left-hand side term of the previous equation is zero.

As external forces, there are the gravity force, acting on the mass inside the CV, and the surface forces, namely the integral of the stresses
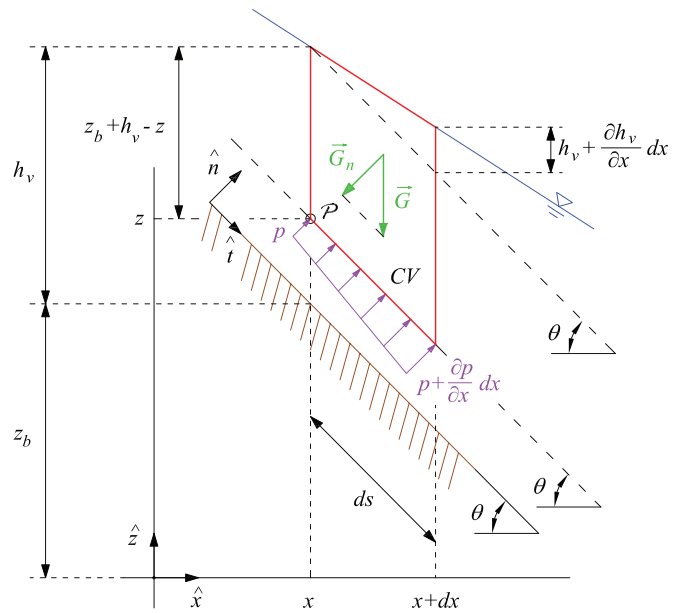

Fig. 3. CV used to derive the pressure distribution along the z-direction.

over each CV surface. Because of the basic assumption provided in Section 2.1, the stress on the free-surface is null while, thanks to the SF conditions, both the shear stresses and the net resultant of the normal stresses along the vertical surfaces are negligible. The normal components of the remaining forces are:

The normal component of the gravity force G_n. The gravity force is directed in the opposite direction of the $\widehat{z}$ unit vector, and its norm is given by ρg times the volume of the CV (trapezoidal-based prism of unit height):

$$\overrightarrow{G} = -\rho g \frac{1}{2} \left[(z_b + h_v - z) + \left(z_b + h_v + \frac{\partial h_v}{\partial x} dx - z \right) \right] dx \widehat{z} =$$
$$- \left[\rho g (z_b + h_v - z) dx + \mathcal{O}((dx)^2) \right] \widehat{z}$$

Considering only the first-order terms, the component G_n becomes:

$$G_n = -\rho g (z_b + h_v - z) \cos\theta \, dx \tag{25}$$

The normal component of the thrust on the lower surface P_n. The thrust $\overrightarrow{P}$ on the lower surface of the CV is given by the integral of the pressure distribution. Since this distribution is linear, the thrust is:

$$\overrightarrow{P} = \frac{1}{2} \left[p + \left(p + \frac{\partial p}{\partial x} dx \right) \right] \frac{dx}{\cos\theta} \widehat{n} = \left[\frac{p}{\cos\theta} dx + \mathcal{O}((dx)^2) \right] \widehat{n} \tag{26}$$

where p is the pressure in $\mathscr{P}(x, z)$ and $dx/\cos\theta$ is the length of the surface ds. Considering only the first order term, the component P_n becomes:

$$P_n = \frac{p}{\cos\theta} dx \tag{27}$$

Using Eqs. (25) and (27), Eq. (24) reduces to:

$$0 = G_n + P_n = -\rho g (z_b + h_v - z) \cos\theta \, dx + \frac{p}{\cos\theta} dx$$

After dividing by dx, we can get the pressure relation:

$$p = \rho g (z_b + h_v - z) \cos^2\theta$$

showing that the distribution increases linearly starting from the free surface. At the bed level $z = z_b$ and the pressure p_b becomes:

$$p_b = \rho g h_v \cos^2\theta \tag{28}$$

3.5. Momentum balance equation in the x-direction

Let us consider the x-momentum $\rho u_x^{'}$, where $u_x^{'}$ is, generically, the local and instantaneous x-velocity. The Lagrangian expression of its balance in the x-direction is:

$$\frac{D}{Dt}\int_{SV}\rho u_x^{'}\,\mathrm{d}V = \sum_i F_x^i \tag{29}$$

where F_x^i represents the x-component of the i-th external force acting on the CV.

By using Eq. (21), setting $a^{'} = \rho u_x^{'}$ and gathering the constant terms $\rho\,\mathrm{d}x$, the left-hand side of the previous equation becomes:

$$\rho\left(\frac{\partial}{\partial t}h_v u_x + \frac{\partial}{\partial x}\alpha_{u_x^2}u_x^2 h_v\right)\mathrm{d}x \tag{30}$$

where $\alpha_{u_x^2}$ is the so-called velocity profile factor evaluated along a vertical section and is given by Eq. (16) in which $a^{'} = u_x^1$. The corresponding term in an LCS is unitary since, according to the Voellmy-fluid assumptions the velocity distribution is constant along the normal direction (Section 2.2). In Appendix A we provide a demonstration that, under reasonable assumptions, even $\alpha_{u_x^2}$ can be assumed to be unitary.

As for the external forces, due to the choice of the reference system, the gravity force has a null component in the x-direction. Nevertheless, the action of the gravity is present through the pressure terms both on the sides and on the bottom of the CV. The surface forces showing x-components, sketched in Fig. 4, are:

The thrusts on the vertical sections. These thrusts, according to the model assumptions, derive from the pressure distribution along the vertical sections and are vectors aligned with the x-axis. Since the pressure distribution is linear, the left-hand thrust can be written as:

$$\overrightarrow{T}_l = \rho g\frac{h_v^2}{2}cos^2\theta\,\,\widehat{x} \tag{31}$$

The right-hand thrust $\overrightarrow{T}_r$ has a norm that can be expressed through a first-order Taylor expansion of the left-hand side thrust norm, while its direction is opposite the x-axis unit vector:
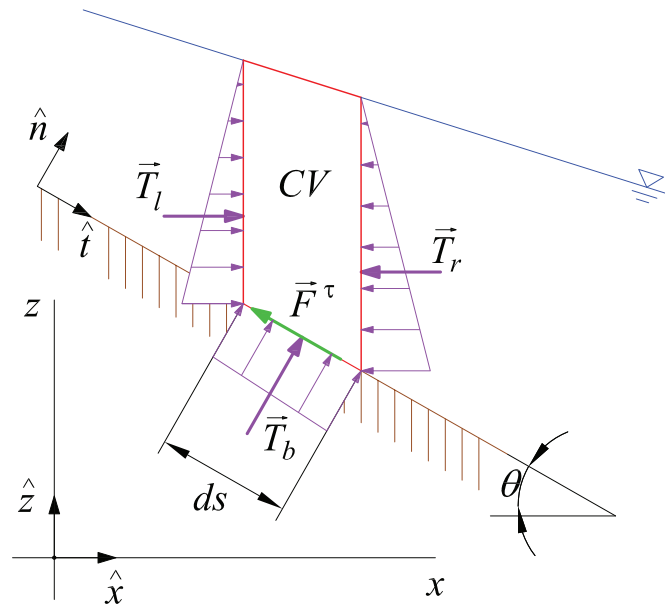

Fig. 4. Forces and stresses distributions on the infinitesimal Control Volume used to derive the x-momentum balance equation.

$$\overrightarrow{T}_r = \left[\rho g\frac{h_v^2}{2}cos^2\theta + \frac{\partial}{\partial x}\left(\rho g\frac{h_v^2}{2}cos^2\theta\right)\mathrm{d}x\right](-\widehat{x})$$

The net thrust in the x-direction becomes:

$$T_{lx} + T_{rx} = -\frac{\partial}{\partial x}\left(\rho g\frac{h_v^2}{2}cos^2\theta\right)\mathrm{d}x \tag{32}$$

The x-component of the bed normal thrust. The bed normal thrust $\overrightarrow{T}_b$ has the direction of the normal to the bed and its norm, to the first order of accuracy, is equal to the bed pressure in x times the length $\mathrm{d}s$ over which the pressure is applied:

$$\overrightarrow{T}_b = \rho g h_v cos^2\theta\,\,\mathrm{d}s\,\,\widehat{n} \tag{33}$$

Considering that $\mathrm{d}s = \mathrm{d}x/cos\,\theta$ and that the Cartesian expression of $\widehat{n}$ is given by Eq. (7), then the x-component of the bed thrust becomes:

$$T_{bx} = \rho g h_v cos\theta sin\theta\,\,\mathrm{d}x \tag{34}$$

To express this term in a way that resembles the relevant term in the classical SW equations, we introduce the bed slope:

$$i_f = tan\theta = -\frac{\partial z_b}{\partial x} \tag{35}$$

and multiplying and dividing Eq. (34) by $cos\theta$, we can express the x-component of the bed thrust term as a function of the bed slope:

$$T_{bx} = -\rho g h_v cos^2\theta\frac{\partial z_b}{\partial x}\,\,\mathrm{d}x \tag{36}$$

The x-component of the bed shear force. The bed shear force is a vector parallel to the bed and its norm, to the first order of approximation, is equal to the bed stress $\overrightarrow{\tau}_0$ evaluated in x, times the length $\mathrm{d}s$ along which the stress is applied. According to Eq. (1), it can be written as:

$$\overrightarrow{F}^\tau = \overrightarrow{\tau}_0\,\,\mathrm{d}s = -\tau_0\,\,\mathrm{d}s\,\,\widehat{s}^\tau \tag{37}$$

Considering that $\mathrm{d}s = \mathrm{d}x/cos\,\theta$, then the x-component of the bed shear force becomes:

$$F_x^\tau = \frac{\tau_{0x}}{cos\theta}\,\,\mathrm{d}x = -\tau_0\frac{s_x^\tau}{cos\theta}\,\,\mathrm{d}x \tag{38}$$

The final x-direction momentum balance equation can be obtained employing Eqs. (30) (with unitary velocity profile factor), (32), (36) and (38) in Eq. (29) and dividing the resulting equation by the constant term $\rho\,\mathrm{d}x$, thus obtaining:

$$\frac{\partial}{\partial t}(h_v u_x) + \frac{\partial}{\partial x}\left(u_x^2 h_v + g cos^2\theta\frac{h_v^2}{2}\right) + g h_v cos^2\theta\frac{\partial z_b}{\partial x} = -\frac{\tau_0}{\rho}\frac{s_x^\tau}{cos\theta} \tag{39}$$

3.6. The Voellmy-fluid friction law in GCS

As for the bed shear stress vector, expressed as in Eq. (1), we have to specify the value of τ_0 and $\widehat{s}^\tau$. According to the assumptions presented in Section 2.2, we have to distinguish the following two cases:

Static case: in this case, the x-component of the bed shear stress τ_{0x} can be computed from Eq. (39) with all the velocity-dependent terms vanishing and, by using Eq. (38), we obtain:

$$\tau_{0x} = \rho cos\theta\left[\frac{\partial}{\partial x}\left(g cos^2\theta\frac{h_v^2}{2}\right) + g h_v cos^2\theta\frac{\partial z_b}{\partial x}\right] \tag{40}$$

As for the z-component, since the bed shear vector is parallel to the bed, it can be obtained imposing that the dot product of the shear stress vector and the unit normal vector given by Eq. (7) is zero, namely $\overrightarrow{\tau}_0\cdot\widehat{n} = 0$. From this, we get:

$$\tau_{0z} = -\tau_{0x} tan\theta \tag{41}$$

Considering the orthogonality between the x- and z-components of the shear stress vector, from the previous equation it is straightforward to obtain:

$$\tau_0 = \left\| \vec{\tau}_0 \right\| = \sqrt{\tau_{0x}^2 + \tau_{0z}^2} = \frac{|\tau_{0x}|}{cos\theta} \tag{42}$$

and, considering the x-component of Eq. (1) and the previous relation, we get:

$$s_x^\tau = -\frac{\tau_{0x}}{\tau_0} = -\frac{\tau_{0x}}{|\tau_{0x}|} cos\theta \tag{43}$$

According to Eq. (2) $\tau_0 \leq \tau_c$, where the bed pressure present in this last term is evaluated by using Eq. (28), thus obtaining:

$$\tau_c = \mu\ \rho g h_v cos^2\theta \tag{44}$$

Dynamic case: the norm of the velocity vector appearing in the Voellmy friction law, Eq. (3), is expressed as a function of the vertical-depth averaged velocity. Since $u_z = -u_x \tan\theta$, then $\|\vec{u}\| = |u_x|/cos\theta$. The final expression for the Voellmy stress is:

$$\frac{\tau_0}{\rho} = \frac{\tau_v}{\rho} = \frac{\tau_c}{\rho} + g\frac{u_x^2}{\xi cos^2\theta} \tag{45}$$

where τ_c is given by Eq. (44). As for the direction, according to Eq. (4) and considering the expression of the velocity norm obtained above, the x-component of the unit vector $\hat{s}^\tau$ becomes:

$$s_x^\tau = \frac{u_x}{|u_x|} cos\theta \tag{46}$$

3.7. The final system

The final system is composed by Eqs. (23) and (39)

$$\begin{cases} \dfrac{\partial h_v}{\partial t} + \dfrac{\partial}{\partial x}(h_v u_x) = 0 \\ \dfrac{\partial}{\partial t}(h_v u_x) + \dfrac{\partial}{\partial x}\left(u_x^2 h_v + g cos^2\theta \dfrac{h_v^2}{2}\right) + g h_v cos^2\theta \dfrac{\partial z_b}{\partial x} = \\ = -\dfrac{\tau_0}{\rho}\dfrac{s_x^\tau}{cos\theta} \end{cases} \tag{47}$$

where τ_0 and s_x^τ are given, respectively, by Eqs. (42) and (43) for the static case and by Eqs. (45) and (46) for the dynamic case.

4. 2D extension

The derivation of the 2D version of the model is not fully retraced but, since it is quite easy to guess the structure of the resulting system, we simply extend the 1D set of equations focusing only on some peculiar elements.

As a first step, we have to set the three-dimensional GCS. It is a Cartesian orthogonal system (see Fig. 5) that, as in the 1D case, has the z-axis opposite to the gravity vector while the x- and y-axis couple is arbitrarily oriented in a horizontal plane.

The second step is to define, in a generic point $\mathscr{P}$ of the bed surface, the tangent plane with respect to which the equations will be defined. Let $F(x,y,z) = z - z_b(x,y) = 0$ a continuous implicit function describing the bed surface, then the unit normal vector is given by $\hat{n} = \vec{\nabla}F/\|\vec{\nabla}F\|$. In terms of components, we have:
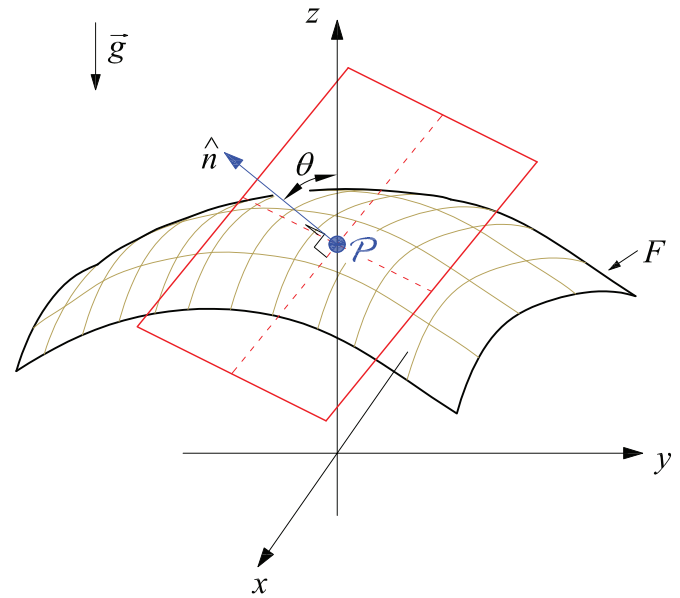

Fig. 5. Sketch of the local tangent plane in $\mathscr{P}$, its relevant geometry and the Global Reference System used for the 2D flow equations.

$$(n_x, n_y, n_z) = \frac{\left(-\frac{\partial z_b}{\partial x}, -\frac{\partial z_b}{\partial y}, 1\right)}{\sqrt{\left(\frac{\partial z_b}{\partial x}\right)^2 + \left(\frac{\partial z_b}{\partial y}\right)^2 + 1}} \tag{48}$$

It is worth noting that:

$$n_z = cos\theta = \frac{1}{\sqrt{\left(\frac{\partial z_b}{\partial x}\right)^2 + \left(\frac{\partial z_b}{\partial y}\right)^2 + 1}} \tag{49}$$

where the angle θ is the angle between the normal direction and the vertical direction (see again Fig. 5), while the other two components can be written as:

$$n_x = -\frac{\partial z_b}{\partial x}n_z; \quad n_y = -\frac{\partial z_b}{\partial y}n_z \tag{50}$$

We will use this result extensively in a while.

Assuming, for simplicity's sake, that $\mathscr{P}$ is located in $(0,0,z_0)$, as in Fig. 5, the relevant tangent plane is described by the following expression:

$$n_x x + n_y y + n_z z = n_z z_0 \tag{51}$$

We direct the reader to Appendix B for the derivation of this expression together with some features of the plane, such as the fact that the angle θ represents the steepest slope angle of the tangent plane.

Third, we have to define the CV. In this case, it is the volume enclosed by four fixed vertical faces, spanning from the bed to the free surface, two of them parallel to the x-z plane and dy apart, the other two parallel to the y-z plane and dx apart, and by the bed and free surface areas limited by said vertical faces. The upper surface moves vertically with the same velocity as the free surface. Similarly to the 1D case, because of the infinitesimal distance between the couples of vertical sections, all the field variables, including the bed elevation, can be expressed with a first-order spatial Taylor expansion. Thus, all variables vary linearly inside the CV and in particular, in the derivation of the equations, we assume that all these variables are positive as x and y increase.

According to the 1D approach, the system of partial differential equations relevant to this CV is composed of the mass balance equation

and the x- and y-momentum balance equations. To obtain this system, we need to specify the following terms.

Bed area of the CV. The bed area of the 2D CV can be represented as $d\vec{A}_s = \hat{n}\,dA_s$ where $\hat{n}$ is the normal to the bed and dA_s is the bed area (see Fig. 6). By construction, the projection of this area on a horizontal plane gives a square of sides $dx\,dy$. This last area can be represented by the vector $d\vec{A} = \hat{z}\,dA$ where $\hat{z}$ is the unit vector of the z-axis and $dA = dx\,dy = n_z dA_s$. From this last relation and considering Eq. (49), we obtain the CV bed area expression:

$$dA_s = \frac{1}{cos\theta}dA \tag{52}$$

Pressure terms. The approach applied for obtaining the pressure distribution along the normal direction and the vertical direction in the 1D case can be applied also to the 2D case. The result shows that the 1D expressions for the bed pressure, Eq. (28), and for the thrust per unit width on a vertical section, Eq. (31), are still valid in the 2D case but, this time, the term $cos\theta$ is given by Eq. (49). Therefore, all the terms concerning the pressure in the 2D model, have the same expression as the respective terms in the 1D case.

Velocity norm. To express the Voellmy friction law, the norm of the vertical-depth averaged velocity $\vec{u} = (u_x, u_y, u_z)$ is needed. Similarly to the 1D case, it is necessary to write an algebraic relation expressing the z-component of the velocity as a function of the x- and y- components. It can be obtained by exploiting the 2D SF condition according to which the velocity vector must lie on a plane parallel to the tangent plane or, equivalently, it must be orthogonal to the normal unit vector of the plane. Mathematically this becomes:

$$\vec{u}\cdot\hat{n} = 0 \tag{53}$$

From this condition, considering also Eq. (50), the searched z-component is:

$$u_z = -\frac{u_x n_x + u_y n_y}{n_z} = \frac{\partial z_b}{\partial x}u_x + \frac{\partial z_b}{\partial y}u_y \tag{54}$$

while the velocity norm becomes:

$$\|\vec{u}\| = \sqrt{u_x^2 + u_y^2 + \left(\frac{\partial z_b}{\partial x}u_x + \frac{\partial z_b}{\partial y}u_y\right)^2} \tag{55}$$

Bed shear stress force. The bed shear stress force acting on the CV is the integral of the bed shear stresses over the area dA_s. To the first order of approximation, it can be written as:

$$\vec{F}^\tau = \vec{\tau}_0\,dA_s = -\tau_0\,dA_s\,\hat{s}^\tau \tag{56}$$

Dividing both sides of this expression by dA and using Eq. (52), the x- and y- components of this force, as they appear in the x- and the y-momentum balance equations, become:
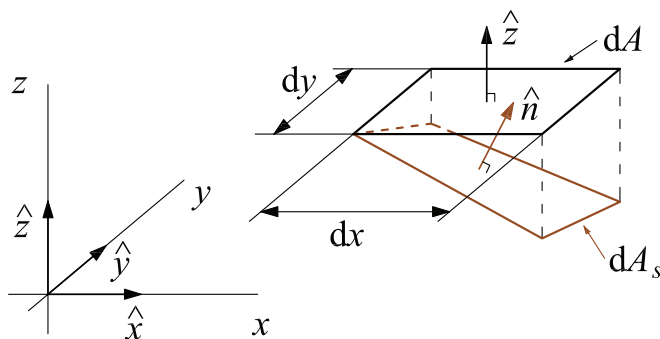

Fig. 6. Sketch of the CV bed area, its horizontal projection and the relevant geometry.

$$\frac{F_x^\tau}{dA} = \frac{\tau_{0x}}{cos\theta} = -\tau_0 \frac{s_x^\tau}{cos\theta} \tag{57}$$

$$\frac{F_y^\tau}{dA} = \frac{\tau_{0y}}{cos\theta} = -\tau_0 \frac{s_y^\tau}{cos\theta} \tag{58}$$

4.1. The flow equations

Considering the expressions derived above, the 2D Partial Differential Equations (PDEs) system can be obtained straightforwardly by extending the system (47) to the 2D case:

$$\begin{cases} \dfrac{\partial h_v}{\partial t} + \dfrac{\partial}{\partial x}\left(u_x h_v\right) + \dfrac{\partial}{\partial y}\left(u_y h_v\right) = 0 \\[2mm] \dfrac{\partial}{\partial t}\left(h_v u_x\right) + \dfrac{\partial}{\partial x}\left(u_x^2 h_v + g\dfrac{h_v^2}{2}cos^2\theta\right) + \dfrac{\partial}{\partial y}\left(u_x u_y h_v\right)+ \\[2mm] \qquad\qquad +gh_v cos^2\theta\dfrac{\partial z_b}{\partial x} = -\dfrac{\tau_0}{\rho}\dfrac{s_x^\tau}{cos\theta} \\[2mm] \dfrac{\partial}{\partial t}\left(h_v u_y\right) + \dfrac{\partial}{\partial x}\left(u_x u_y h_v\right) + \dfrac{\partial}{\partial y}\left(u_y^2 h_v + g\dfrac{h_v^2}{2}cos^2\theta\right)+ \\[2mm] \qquad\qquad +gh_v cos^2\theta\dfrac{\partial z_b}{\partial y} = -\dfrac{\tau_0}{\rho}\dfrac{s_y^\tau}{cos\theta} \end{cases} \tag{59}$$

It is worth noting that the contributes of the averaged transverse shear stresses, namely $\partial(h_v\tau_{yx})/\partial y$ and $\partial(h_v\tau_{xy})/\partial x$, do not appear respectively in the x- and y-momentum equations, because thanks to the SF conditions they are negligible compared to the other terms.

4.2. The 2D Voellmy-fluid friction law in GCS

The 1D Voellmy-fluid friction law, presented in Section 3.6, must also be extended to the 2D case.

Static case: the horizontal components of the bed shear stress vector can be obtained from the x- and y- momentum equations of system (59) with all the velocity-dependent terms vanishing. Using Eq. (57) and (58) we can get:

$$\tau_{0x} = \rho cos\theta\left[\frac{\partial}{\partial x}\left(g\frac{h_v^2}{2}cos^2\theta\right) + gh_v cos^2\theta\frac{\partial z_b}{\partial x}\right] \tag{60}$$

$$\tau_{0y} = \rho cos\theta\left[\frac{\partial}{\partial y}\left(g\frac{h_v^2}{2}cos^2\theta\right) + gh_v cos^2\theta\frac{\partial z_b}{\partial y}\right] \tag{61}$$

As for the z-component, it can be obtained, as done for the velocity vector, imposing $\vec{\tau}_0\cdot\hat{n} = 0$. From this, we get:

$$\tau_{0z} = \frac{\partial z_b}{\partial x}\tau_{0x} + \frac{\partial z_b}{\partial y}\tau_{y0}$$

Knowing the three components, it is straightforward to obtain the norm of the bed shear stress τ_0 and, according to Eq. (1) the unit vector components $s_x^\tau = -\tau_{0x}/\tau_0$; $s_y^\tau = -\tau_{0y}/\tau_0$ appearing in the system (59).

Dynamic case: in this case, the norm of the shear stress vector is given by the Voellmy friction law:

$$\frac{\tau_0}{\rho} = \frac{\tau_v}{\rho} = \frac{\tau_c}{\rho} + g\frac{\|\vec{u}\|^2}{\xi} \tag{62}$$

As for the direction, we assume that there is no lag between the bed shear stress and the depth-averaged velocity vector. Therefore, we can write:

$$\hat{s}^\tau = \frac{\vec{u}}{\|\vec{u}\|} \tag{63}$$

5. Numerical approach

Since the main goal of this work is obtaining a robust modelling tool, particular attention has been paid to set up the numerical method. The following subsections are devoted to presenting, in a synthetic way, the main points of this approach. More details can be found in the papers cited inside each Section. As explained in the Introduction, this approach resembles the methodology employed in the TRENT2D model (Armanini et al., 2009).

The novel aspect presented here is the effective treatment of static conditions enabled by the velocity-independent term of the Voellmy friction law. This was achieved by developing a particular algorithm for dealing with the source terms of the PDEs (Section 5.4), and with the static case with free-surface gradients (Section 5.5).

5.1. The system of equations and its hyperbolic nature

In system (59), the bed elevation is not a field variable and therefore, the terms involving its spatial derivatives are source terms. In this framework, the bed cannot present discontinuities because in these cases the spatial derivatives lose their meaning. However, since we want to deal with cases in which the bed shows discontinuities, following the strategy employed by several authors (see e.g., LeFloch and Thanh, 2007; Rosatti and Begnudelli, 2010; Parés and Pimentel, 2019), the bed level z_b is considered a field variable and an additional differential equation, namely $\partial z_b/\partial t = 0$, is added to the original system of PDEs (59) to guarantee that the bed is fixed. As demonstrated below, the homogeneous part of this "augmented" system is hyperbolic and therefore admits discontinuous solutions involving all the variables, including z_b. However, due to the additional equation, the position and the magnitude of the bed discontinuity does not change.

Thanks to this mathematical feature, a suitable numerical scheme can treat automatically both bed steps in the flow direction and side bed steps. It is worth noting that the resulting system is nonconservative i.e., a system in which spatial derivatives of terms involving filed variables are multiplied by expressions which, in turn, include field variables. In this case, the relations valid across discontinuities of the solutions are not the standard Rankine-Hugoniot relations but the Generalized Rankine-Hugoniot ones that present one more term compared to the standard case (see Rosatti and Zugliani, 2015).

The augmented system can be written in compact form as:

$$\frac{\partial \mathbf{U}}{\partial t} + \frac{\partial \mathbf{F}}{\partial x} + \frac{\partial \mathbf{G}}{\partial y} + \boldsymbol{\Gamma}_x \frac{\partial z_b}{\partial x} + \boldsymbol{\Gamma}_y \frac{\partial z_b}{\partial y} = \mathbf{S} \quad (64)$$

where

$$\mathbf{U} = \begin{bmatrix} h_v \\ u_x h_v \\ u_y h_v \\ z_b \end{bmatrix}; \quad \mathbf{F} = \begin{bmatrix} u_x h_v \\ u_x^2 h_v + g\frac{h_v^2}{2}cos^2\theta \\ u_x u_y h_v \\ 0 \end{bmatrix}$$

$$\mathbf{G} = \begin{bmatrix} u_y h_v \\ u_x u_y h_v \\ u_y^2 h_v + g\frac{h_v^2}{2}cos^2\theta \\ 0 \end{bmatrix}$$

are, respectively, the vectors of the conserved variables and conservative fluxes in the x- and y-directions, while

$$\boldsymbol{\Gamma}_x = \begin{bmatrix} 0 & gh_v cos^2\theta & 0 & 0 \end{bmatrix}^T; \quad \boldsymbol{\Gamma}_y = \begin{bmatrix} 0 & 0 & gh_v cos^2\theta & 0 \end{bmatrix}^T$$

represent the vectors of non-conservative terms for the two coordinate directions and

$$\mathbf{S} = \begin{bmatrix} 0 \\ -\dfrac{\tau_0}{\rho}\dfrac{s_x^\tau}{cos\theta} \\ -\dfrac{\tau_0}{\rho}\dfrac{s_y^\tau}{cos\theta} \\ 0 \end{bmatrix} \quad (65)$$

is the source terms vector.

The hyperbolic nature of the homogeneous part of the system (64) is analysed by considering a plane-wave problem in a given direction (see e.g., Toro, 2009, among many). To provide a general expression, we consider a generic horizontal reference system (π, ν), where π is the longitudinal direction of the plane-wave problem and ν is the transversal, normal-to-π direction. With respect to this reference system, the problem is described by:

$$\frac{\partial \mathbf{U}_\pi}{\partial t} + \frac{\partial \mathbf{F}_\pi}{\partial \pi} + \boldsymbol{\Gamma}_\pi \frac{\partial z_b}{\partial \pi} = \mathbf{0} \quad (66)$$

where

$$\mathbf{U}_\pi = \begin{bmatrix} h_v \\ u_\pi h_v \\ u_\nu h_v \\ z_b \end{bmatrix}; \quad \mathbf{F}_\pi = \begin{bmatrix} u_\pi h_v \\ u_\pi^2 h_v + g\frac{h_v^2}{2}cos^2\theta \\ u_\pi u_\nu h_v \\ 0 \end{bmatrix}$$

$$\boldsymbol{\Gamma}_\pi = \begin{bmatrix} 0 \\ gh_v cos^2\theta \\ 0 \\ 0 \end{bmatrix}$$

The eigenvalues are:

$$\lambda_1 = u_\pi - cos\theta\sqrt{gh_v}; \ \lambda_2 = 0$$
$$\lambda_3 = u_\pi; \ \lambda_4 = u_\pi + cos\theta\sqrt{gh_v} \quad (67)$$

while the associated eigenvectors are:

$$\mathbf{R}_1 = \begin{bmatrix} 1 \\ u_\pi - \sqrt{gh_v}\,cos\theta \\ u_\nu \\ 0 \end{bmatrix}; \quad \mathbf{R}_2 = \begin{bmatrix} gh_v cos^2\theta \\ 0 \\ gh_v u_\nu cos^2\theta \\ u_\pi^2 - gh_v cos^2\theta \end{bmatrix}$$

$$\mathbf{R}_3 = \begin{bmatrix} 0 \\ 0 \\ 1 \\ 0 \end{bmatrix}; \quad \mathbf{R}_4 = \begin{bmatrix} 1 \\ u_\pi + \sqrt{gh_v}\,cos\theta \\ u_\nu \\ 0 \end{bmatrix}$$

Since there is a full set of eigenvalues and associated eigenvectors, the PDEs system (64) is hyperbolic. This property allows us to use, as a numerical integration strategy, a finite volume method with Godunov fluxes as described below.

5.2. The discretization of the homogeneous equations

Space is discretized with a regular Cartesian grid composed of square cells of area $A_{i,j} = \Delta x \Delta y$, whose sides are aligned with the x and y axis. In a finite volume framework, according to the MUSCL-Hancock approach (for details, see e.g., Toro, 2009, Section 14.4), field variables inside the cells are approximated with piecewise linear functions and then they are evolved in time for a half time step with a nonconservative method, to obtain guess values to be used in the subsequent conservative step (see Fig. 7(a)). To avoid spurious oscillations, in the spatial reconstruction a
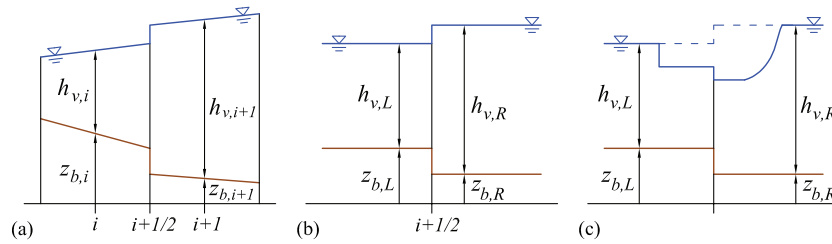
Fig. 7. (a) Piecewise linear reconstruction of the primitive variables inside the cells; (b) Riemann problem arising at the cell interface; (c) possible solution of the Riemann problem at the cell interface.

minmod slope limiter (see e.g. Toro, 2009, Section 14.4.3) is used.

In the conservative step, we integrate the homogeneous part of Eq. (64) in time over an interval Δt and in space over cell i, j obtaining:

$$
\begin{aligned}
\widehat{\mathbf{U}}_{i,j} = \; & \mathbf{U}_{i,j}^n - \frac{\Delta t}{\Delta x}\left(\mathbf{f}_{i+1/2,j}^- - \mathbf{f}_{i-1/2,j}^+\right) - \frac{\Delta t}{\Delta y}\left(\mathbf{g}_{i,j+1/2}^- - \mathbf{g}_{i,j-1/2}^+\right) \\
& - \frac{\Delta t}{\Delta x}[\mathbf{\Upsilon}_x]_{i,j}^{n+1/2}\left((z_b)_{i+1/2,j} - (z_b)_{i-1/2,j}\right) \\
& - \frac{\Delta t}{\Delta y}[\mathbf{\Upsilon}_y]_{i,j}^{n+1/2}\left((z_b)_{i,j+1/2} - (z_b)_{i,j-1/2}\right)
\end{aligned}
\tag{68}
$$

where, with the subscript i, j we indicate a cell-averaged value, conventionally assigned to the centre of the i, j cell, while $\mathbf{f}_{i+1/2,j}^\pm$ and $\mathbf{g}_{i,j+1/2}^\pm$ are the total fluxes evaluated at time step $n + 1/2$ on the left (minus superscript) and on the right (plus superscript) of a cell boundary, along the x and y direction respectively. These total fluxes comprise both the discretization of the conservative fluxes $\mathbf{F}$, $\mathbf{G}$ and the non-conservative ones $\Gamma_x \partial z_b / \partial x + \Gamma_y \partial z_b / \partial x$. It should be noted that in case of bed discontinuities, the left and right values are different because of the non-conservative fluxes contribute. Finally, $\widehat{\mathbf{U}}_{i,j}$ represents the evolution of the conserved vector without the effect of the source term. Therefore, it is an approximated expression of the conserved variable vector at time $n + 1$ that will be corrected in a subsequent step, as specified further on.

The scheme as a whole is second-order accurate both in space and time and since it is explicit and the conserved variables are updated considering both spatial directions simultaneously, its CFL stability condition reads:

$$
C_R = |\lambda|_{max} \frac{\Delta t}{\Delta x} \le 0.5 \tag{69}
$$

where $|\lambda|_{max}$ is the maximum modulus of the eigenvalues expressed by Eq. (67) evaluated for all cells at time n. In our model, we set $C_R = 0.45$ and we compute the relevant time step accordingly.

5.3. The Riemann solver

In the framework of the finite-volume methods, the Godunov-type fluxes are obtained from the solution of plane-wave Riemann Problems (RPs) arising at the interfaces of the cells because of the reconstruction algorithm (see Fig. 7(b)).

The mathematical expression of a RP, written for ease of notation with respect to the (π, ν) system with the origin located on the middle of a given cell interface and with the direction π normal to the interface, is:

$$
\begin{cases}
\dfrac{\partial \mathbf{U}_\pi}{\partial t} + \dfrac{\partial \mathbf{F}_\pi}{\partial \pi} + \Gamma_\pi \dfrac{\partial z_b}{\partial \pi} = 0 \\[2mm]
\mathbf{U}_\pi(\pi 0) = \begin{cases} \mathbf{U}_{\pi L} & \text{if } \pi \le 0 \\ \mathbf{U}_{\pi R} & \text{if } \pi > 0 \end{cases}
\end{cases}
\tag{70}
$$

where the initial values $\mathbf{U}_{\pi L}$ and $\mathbf{U}_{\pi R}$ are the left and right reconstructed values with respect to the cell interface. The solution to this initial value

problem is "simple", in the sense that it is composed only of shocks, rarefactions and constant state fields (see Fig. 7(c)). Once the solution is obtained, the numerical fluxes to be used in Eq. (68) derive from the flux vector of the RP solution evaluated in $\pi = 0$.

However, since the analytical solution of a RP can be computationally expensive, an approximate solution algorithm, called Riemann solver, is commonly employed. In our work, we chose the one proposed by Zugliani and Rosatti (2016) (extension of the DOT algorithm developed by Dumbser and Toro (2011a, 2011b)). Denoted with $\mathbf{Q}_\pi^\pm$ the total flux vector in a generic direction, such that if $\pi = x$ then $\mathbf{Q}_\pi^\pm = \mathbf{f}_{i-1/2,j}^\pm$ while if $\pi = y$ then $\mathbf{Q}_\pi^\pm = \mathbf{g}_{i,j+1/2}^\pm$, the expression for the flux vector is:

$$
\mathbf{Q}_\pi^\pm = \frac{1}{2}(\mathbf{Q}_L + \mathbf{Q}_R) - \frac{1}{2}(\pm \mathbf{D}) - \frac{1}{2}\left(\int_0^1 |\mathscr{A}(\Psi(s))|\, \mathbf{B}(\Psi(s))\frac{\partial \Psi}{\partial s}\, ds\right) \tag{71}
$$

where:

$$
\Psi(s) = \mathbf{W}_L + s(\mathbf{W}_R - \mathbf{W}_L) \tag{72}
$$

is the linear path, in the phase space, connecting the left and right RP values of the field variables expressed by the vectors:

$$
\mathbf{W}_{L,R} = [\, h_v \quad u_\pi \quad u_\nu \quad z_b \,]_{L,R}^T; \tag{73}
$$

$\mathbf{Q}_{L, R}$ are the conservative left and right RP vector fluxes:

$$
\mathbf{Q}_{L,R} = \begin{bmatrix} u_\pi h_v \\ u_\pi^2 + g\cos^2\theta\, \dfrac{h_v^2}{2} \\ u_\pi u_\nu h_v \\ 0 \end{bmatrix}_{L,R}; \tag{74}
$$

$|\mathscr{A}|$ is evaluated as $\mathcal{R}|\Lambda|\mathcal{R}^{-1}$ where $|\Lambda|$ is the diagonal matrix whose elements are the absolute values of the eigenvalues, $\mathcal{R}$ is the matrix whose columns are composed by the eigenvectors and $\mathcal{R}^{-1}$ is its inverse; finally, $\mathbf{B} = \partial \mathbf{U}/\partial \mathbf{W}$ is the Jacobian matrix of the conserved variables expressed in terms of the primitive ones and $\mathbf{D} = [\,0 \quad T_{bs} \quad 0 \quad 0\,]^T$ where T_{bs} expresses the thrust exerted by the fluid on the bed discontinuity (see Rosatti and Fraccarollo, 2006) whose value is:

$$
\begin{aligned}
& T_{bs} = -g\left(h_{v,k} - \frac{|z_{b,R} - z_{b,L}|}{2}\right)(z_{b,R} - z_{b,L}) \\
& k = \begin{cases} L & \text{if } z_{b,L} \le z_{b,R} \\ R & \text{otherwise} \end{cases}
\end{aligned}
\tag{75}
$$

This thrust is nothing but the additional term in the Generalized Rankine-Hugoniot relations compared to the standard case. Its presence inside the Riemann solver allows the treatment of bed discontinuities and guarantees that the numerical scheme is well-balanced, namely preserves numerical solutions free from spurious effects in situations such as the case of fluid at rest with horizontal free-surface or the uniform flow condition.

5.4. Accounting for the source term

Accounting for the source term is obtained through the operator splitting technique: once the approximated vector of the conserved variables $\widehat{\mathbf{U}}$ has been obtained, it can be "corrected" by applying the source term $\mathbf{S}$ for the given timestep. Mathematically, this operation consists of the integration, over the time step Δt, of the following initial value problem, consisting of a first-order ordinary differential equations system:

$$\begin{cases} \dfrac{d}{dt}\mathbf{U}_{i,j} = \mathbf{S}_{i,j} \\ \mathbf{U}_{i,j}(0) = \widehat{\mathbf{U}}_{i,j} \end{cases} \tag{76}$$

To avoid a limit in the time steps in addition to the one deriving from the Courant condition, Eq. (69), following Armanini et al. (2009), the implicit Euler method is used:

$$\mathbf{U}_{i,j}^{n+1} = \widehat{\mathbf{U}}_{i,j} + \Delta t \mathbf{S}_{i,j}^{n+1} \tag{77}$$

where $U_{i,j}^{n+1}$ is the searched value of the conserved variable vector at the timestep $n + 1$.

The first component of the source vector, Eq. (65), is zero. This means that the value of the first term of $U_{i,j}^{n+1}$, namely $(h_v)_{i,j}^{n+1}$, is obtained directly from Eq. (68). The second and the third equation of Eq. (77) constitute a reduced system:

$$\left(\widetilde{\mathbf{U}_{i,j}^{n+1}}\right) = \left(\widetilde{\widehat{\mathbf{U}}_{i,j}}\right) + \Delta t \left(\widetilde{\mathbf{S}_{i,j}^{n+1}}\right) \tag{78}$$

that expresses nothing but the impulse-momentum theorem divided by ρ.

According to the Voellmy friction law, the source term can be split into a known Coulomb part, indicated with $\left(\widetilde{\mathbf{S}_{i,j}^{n+1}}\right)_\mu$, $(h_v)_{i,j}^{n+1}$ being a known value, and into a velocity-dependent part, indicated with $\left(\widetilde{\mathbf{S}_{i,j}^{n+1}}\right)_\xi$, in which the velocity components at time $n + 1$ are unknowns. The reduced system can be rewritten as:

$$\left(\widetilde{\mathbf{U}_{i,j}^{n+1}}\right) - \Delta t \left(\widetilde{\mathbf{S}_{i,j}^{n+1}}\right)_\xi = \left(\widetilde{\widehat{\mathbf{U}}_{i,j}}\right) + \Delta t \left(\widetilde{\mathbf{S}_{i,j}^{n+1}}\right)_\mu \tag{79}$$

where in the left-hand side terms there are unknown velocity components while in the right-hand side terms there are known values. To solve the system, we have to distinguish between the case where the flow stops and the case where it doesn't. This can be done in the following way:

1. if $\left\| \left(\widetilde{\widehat{\mathbf{U}}_{i,j}}\right) \right\| \leq \Delta t \left\| \left(\widetilde{\mathbf{S}_{i,j}^{n+1}}\right)_\mu \right\|$, where $\left\| \left(\widetilde{\mathbf{S}_{i,j}^{n+1}}\right)_\mu \right\| = \dfrac{\tau_c}{\rho} \dfrac{\sqrt{s_x^{\tau 2} + s_y^{\tau 2}}}{\cos\theta}$ and s_x^τ and s_y^τ are estimated using $\left(\widetilde{\widehat{\mathbf{U}}_{i,j}}\right)$, then the velocity components at time $n + 1$ are identically zero;

2. if $\left\| \left(\widetilde{\widehat{\mathbf{U}}_{i,j}}\right) \right\| > \Delta t \left\| \left(\widetilde{\mathbf{S}_{i,j}^{n+1}}\right)_\mu \right\|$, then Eq. (79) becomes a nonlinear system in terms of velocity components at time $n + 1$, a system that can be solved similarly as in Armanini et al. (2009), namely: a) reducing the system, by appropriately squaring the equations and by adding them, to a single nonlinear equation in which the unknown is the velocity norm at time $n + 1$; b) solving this last equation with a Newton-Raphson method; c) computing velocity components by using Eq. (79) in which the velocity norm is now known.

5.5. The static case with free surface gradients

Thanks to the well-balanced nature of the Riemann solver employed, the strategy described above works well for dynamic conditions and static conditions associated with horizontal free surfaces. Nevertheless, it fails in static cases when the minmod slope limiter produces, across a cell interface, a discontinuity in h_v such that the corresponding free-surface jump is smaller than a threshold value depending on μ (as will we shown below). In these cases, the solver gives fluxes that are not correctly balanced by the source term and an unphysical movement is produced. A solution to this problem can be based on the following predictor-corrector procedure:

Individuation of the critical interfaces. We call a critical interface an interface across which there is a non-null free-surface jump and its value is lower that a threshold value. This value and the interfaces across which this occurs can be individuated in the following way. Let us consider the equations of a purely 1D flow in the normal direction π, where the static condition of null velocity and the limiting value of the bed shear stress norm, namely τ_c, is introduced. The relevant system becomes:

$$\begin{cases} \dfrac{\partial h_v}{\partial t} = 0 \\ \left| \dfrac{\partial}{\partial \pi}\left(g\cos^2\theta \dfrac{h_v^2}{2}\right) + g h_v \cos^2\theta \dfrac{\partial z_b}{\partial \pi} \right| = g h_v \mu \cos^2\theta \end{cases} \tag{80}$$

The first equation simply states that the snow depth cannot change in time while the second expresses the static condition, namely a balance between aligned forcing and resisting actions. Assuming a local constant value of θ, the second equation can be conveniently rewritten in non-conservative form and, introducing the free-surface elevation $\eta = h_v + z_b$ we get:

$$\left| \dfrac{\partial \eta}{\partial \pi} \right| = \mu$$

This expression gives the upper limiting condition and all the slopes lower than μ ensure static conditions.

The expression able to individuate a critical interface can be written, in terms of slopes, as:

$$\left| \dfrac{\partial \eta}{\partial \pi} \right| \leq \mu, \ \cup \ u_\pi = 0 \tag{81}$$

while, in discrete form and in terms of free-surface jumps, as:

$$\left| (z_b + h_v)_R - (z_b + h_v)_L \right| \leq \mu \Delta x \cup \\ (u_\pi)_L = (u_\pi)_R = 0 \tag{82}$$

where here L, R indicates the cell-centred values of the cells located on the left and the right of the interface respectively.

Forcing a no-mass flux condition. On the critical interfaces, the initial conditions of the RPs are forced in such a way as to guarantee no mass flux. This condition, equivalent to an impermeable boundary condition for both sides of the interface, can be obtained by splitting the RP into two RPs, one relevant to the left side and one relevant to the right side of the interface, and imposing a reflective condition in both RPs. This condition is defined as:

$$\begin{cases} \dfrac{\partial \mathbf{U}}{\partial t} + \dfrac{\partial \mathbf{F}}{\partial \pi} + \boldsymbol{\Gamma}_\pi \dfrac{\partial z_b}{\partial \pi} = 0 \\ \mathbf{U}(\pi 0) = \left\{ \begin{bmatrix} h_v \\ u_\pi h_v \\ z_b \end{bmatrix} \text{ for } \pi \leq 0 \ \cup \ \begin{bmatrix} h_v \\ -u_\pi h_v \\ z_b \end{bmatrix} \text{ for } \pi > 0 \right\} \end{cases} \tag{83}$$

where, as usual, the local π-coordinate has its origin at the cell interface and its direction is normal to the interface.

6. Test cases

Test cases have been designed to assess the capabilities of the TRENT2D$^{\circledast}$ numerical model:

- the ability to correctly deal with vertical walls emerging from the flow has been tested with the snow pool test and a straight channel test;
- the accuracy of the overall numerical algorithm has been tested under fully dynamic conditions in a 1D channel flow aligned with an axis direction;
- the correct implementation of the numerical scheme in the 2D case has been verified considering a straight channel flow sloping in a direction rotated with respect to the reference horizontal axes;
- the algorithm for the accounting of the source term under particular conditions have been verified taking into account static cases with free surface gradients and several cases of flow stoppage;
- the ability to cope with submerged bed steps has been analysed with a test in which several retarding structures are submerged during the flow.

Flow cases with analytical solutions have been preferred since they allow to evaluate quantitatively the absolute or the relative errors of the numerical solution compared to the exact one. In the majority of these cases the solution is trivial while, for the 1D channel flow, an analytical solution has been specially developed. To make the assessment more significant, in several cases we have also compared the numerical results of the proposed model with the numerical results obtained with a popular commercial code using an LCS and a specific stopping criterion, namely RAMMS::AVALANCHE (version 1.7.20) (Christen et al., 2008, 2010). For more details on this model, we address the reader to the model site (RAMMS::AVALANCHE, 2021). For the sake of brevity, in the following sections, this model is referred to simply as RAMMS2D.

6.1. Tests with vertical walls emerging from the flow

The first test of this group is one of the classical tests used to evaluate the $\mathscr{C}$-property, namely the capability of a numerical scheme to keep at rest a fluid confined by vertical walls and with a horizontal free surface. The second test concerns the flow in a straight 1D channel with constant width and vertical sidewalls. In this case, while there is motion in the longitudinal direction, the transversal velocity is null and the free surface is static and horizontal in the transverse direction.

6.1.1. Snow pool test

The test consists of considering the "flow" in a square pool of 19 m sides with 10 m vertical walls and flat bottom, filled with a constant

snow depth of 3 m (see Fig. 8). As Voellmy parameters we have chosen μ = 0.1 and ξ = 3000 m/s^2. The cell size was taken equal to 1 m.

Since there are no free-surface gradients and the initial velocity is null, the solution consists of a constant condition equal to the initial condition (i.e. null velocity and constant depth).

Fig. 9 shows the comparison between the exact solution along the central section of the pool (the red dot-dashed plane in Fig. 8) and the numerical solution obtained, after t = 5 s, with TRENT2D$^{\circledast}$ and with RAMMS2D for the free-surface elevation η (top plot) and the norm of the velocity (bottom plot). The proposed model correctly maintains the initial condition indefinitely while the other model generates a non-physical movement of the snow which overtops the side walls.

6.1.2. Straight channel test: cross-sectional flow characteristics

Given a constant slope straight channel with uniform width and vertical sidewalls, the test consists of releasing a prism of snow with constant height, a given longitudinal length and width equal to the width of the channel. Because of the regularity of the flow domain and the initial conditions, the resulting flow is a pure 1D and no variation is expected in the cross-sectional direction. In this test, we are only interested in this last feature, while a more compete dynamical analysis in the longitudinal direction is presented in the next Section.

The channel we considered is 400 m long, 198 m large, aligned with the x-axis, with a constant slope equal to 15° and with vertical walls 10 m high. The release area has a horizontal length equal to 180 m, a normal depth h^0 = 1 m and its upper border is located 40 m downslope the upper end of the channel (see Fig. 10). The side walls are considered frictionless while, as friction parameters for the bed, we have chosen μ = 0.23 and ξ = 2000 m/s^2. The flow domain has been discretized with cells of side equal to 2 m.

In Fig. 11, the free-surface elevation and the velocity norm along a half channel cross section are plotted for TRENT2D$^{\circledast}$ and RAMMS2D. The proposed model accounts correctly for the vertical walls also in this test, while the other model presents variations of the field variables in the cross-sectional direction and an unphysical overtopping. Analogous results are obtained considering cross sections in different spatial positions and at different times.

6.2. Straight channel tests: longitudinal flow features

As can be seen from Fig. 10, the test described in Section 6.1.2 is characterized, in the longitudinal direction, by a flow that presents a front and a tail whose length increases in time, and a core whose length decreases in time. This core shows a depth that is constant in space and time, and a velocity norm that is constant in space but variable in time. If the initial prism is sufficiently long, the core is subjected to a uniformly accelerated flow approaching asymptotically a uniform and permanent
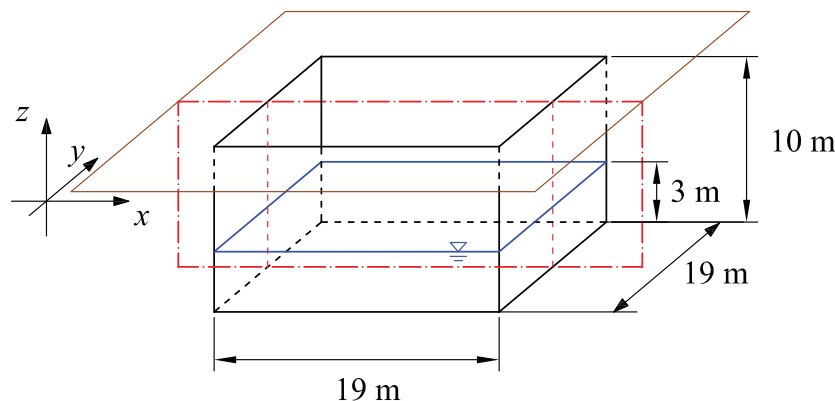

Fig. 8. Sketch of the snow pool test with its geometry. The red dot-dashed line represents the vertical plan used to visualize the test results in Fig. 9. (For interpretation of the references to colour in this figure legend, the reader is referred to the web version of this article.)
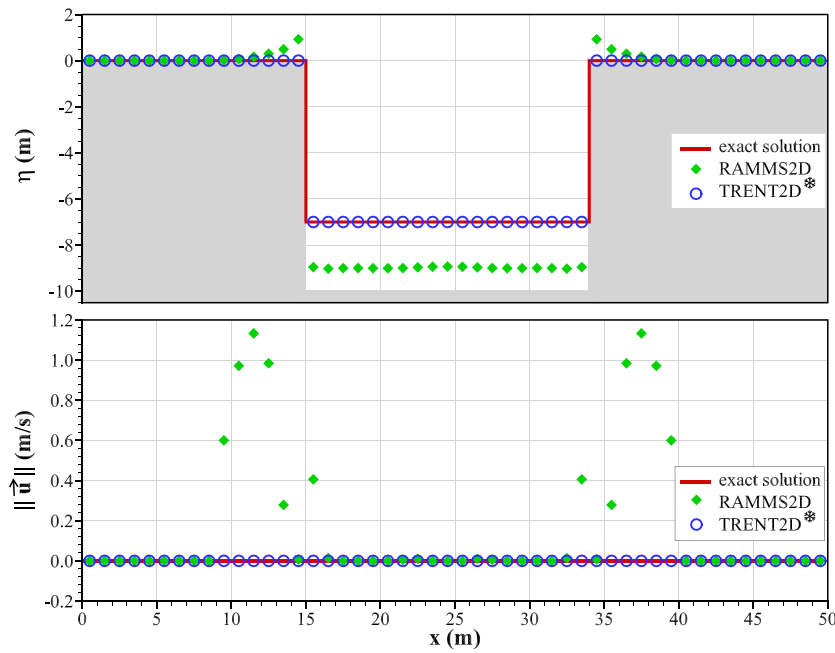
Fig. 9. Results of the snow pool test after $t = 5$ s in a central section. Top plot: free-surface elevation $\eta = z_b + h_v$ and, in grey, the area below the bed surface z_b; bottom plot: the norm of the velocity vector.
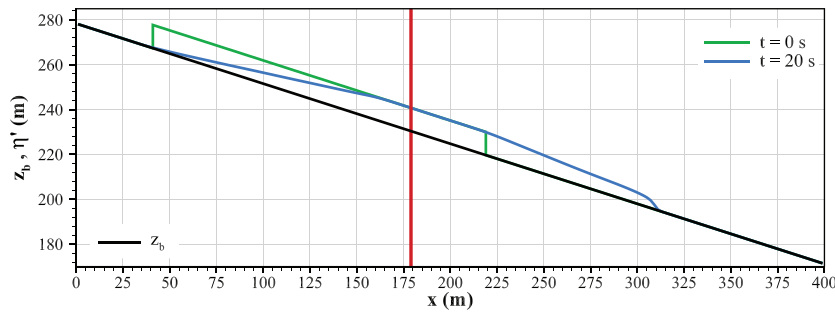

Fig. 10. Longitudinal section of the straight channel test at two different times. To make the snow profile visible, we plotted $\eta' = z_b + 10h_v$. The red line is the trace of the cross section used in Fig. 11. (For interpretation of the references to colour in this figure legend, the reader is referred to the web version of this article.)

flow condition. As shown below, this problem presents an analytical solution.

6.2.1. Analytical solution for core movement

The analytical solution for the core movement can be derived considering a pure 1D flow, namely system (47), where the uniform flow condition $\partial/\partial x = 0$, the positivity of the flow $u_x > 0$ and the bed shear stress expression for the dynamic case apply. The resulting system, here written referring to a generic longitudinal direction π, is:

$$\begin{cases} \dfrac{\partial h_v}{\partial t} = 0 \\ \dfrac{\partial}{\partial t}(h_v u_\pi) = g h_v i_f \cos^2\theta - g h_v \mu \cos^2\theta - g \dfrac{u_\pi^2}{\xi \cos^2\theta} \end{cases}$$

where $i_f = -\partial z_b/\partial\pi$. The first equation, considering the assumption that h_v does not change in space, states the invariance of the snow vertical depth. With this condition, the second equation can be divided by h_v and can be rewritten as a total derivative, since no space variation remains:

$$\frac{d u_\pi}{d t} = a_1 - a_2 u_\pi^2 \tag{84}$$

where $a_1 = g\cos^2\theta(i_f - \mu)$ and $a_2 = g/(h_v\xi\cos^2\theta)$ are two constant whose

units of measure are (m/s^2) and (1/m) respectively. When $t \to \infty$, the time derivative is null and the uniform permanent flow is reached:

$$u_\pi^\infty = \sqrt{\frac{a_1}{a_2}} = \cos^2\theta\sqrt{(i_f - \mu)h_v\xi} \tag{85}$$

By using the previous relation, we can express a_2 as $a_2 = a_1/u_\infty^2$ so Eq. (84) can be rewritten as:

$$\frac{d u_x}{d t} = a_1\left(1 - \left(\frac{u_\pi}{u_\pi^\infty}\right)^2\right) \tag{86}$$

We can introduce now the characteristic time scale of the motion as:

$$t_a = \frac{u_x^\infty}{a_1} = \frac{1}{\sqrt{a_1 a_2}} = \frac{1}{g}\sqrt{\frac{h_v\xi}{i_f - \mu}}$$

and the non-dimensional velocity $u_\pi^* = u_\pi/u_\pi^\infty$ and time $t^* = t/t_a$. The dimensionless form of Eq. (86) is then obtained by dividing the equation by a_1 and multiplying and dividing the left-hand side term by u_π^∞. The result is:
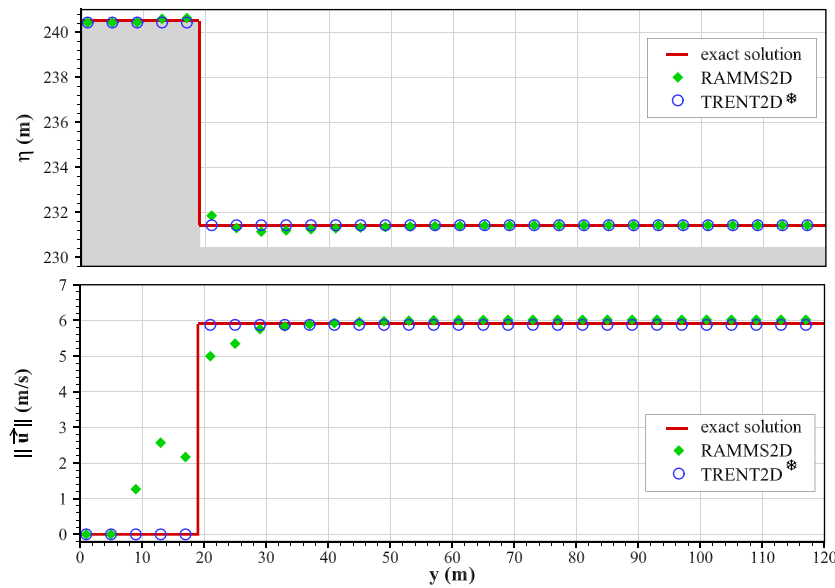
$$\frac{d u_\pi^*}{d t^*} = 1 - u_\pi^{*2} \tag{87}$$

Fig. 11. Half channel cross section, located at $x = 179$ m, of the straight channel test at $t = 20$ s. Top plot: free-surface elevation $\eta = z_b + h_v$ and, in grey, the area below the bed surface z_b; bottom plot: the norm of the velocity vector.

whose solution, considering as initial condition $u_\pi^* = 0$ at $t^* = 0$, is:

$$u_\pi^*(t^*) = tanh t^*$$

This solution shows that the uniform and permanent flow condition is reached at infinite times. Nevertheless, for $t^* = 3$, $u_\pi^* = 0.995$ and therefore, this time can be conventionally considered as the time at which the uniform permanent flow is reached.

6.2.2. Straight channel sloping in the y-axis direction

In this test, the channel direction π is aligned with the y-axis. The angles that the bed channel plan forms with the horizontal reference axes are $\alpha_x = 0°$ and $\alpha_y = 40°$. The angle that the bed normal forms with the vertical axis, defined by Eq. (49) and evaluated with Eq. (B.5), is $\theta = 40°$. The release prism is 324 m long in the π-direction, has a width equal to the channel width and its normal depth is $h^0 = 1.5$ m (to which corresponds a vertical depth $u_v^0 = 1.958$ m). As friction parameters, we have chosen $\mu = 0.2$ and $\xi = 2000$ m/s^2. With this data we obtain $t_a = 7.98$ s, $u_\pi^\infty = 29.36$ m/s while the velocity norm, evaluated with Eq. (55), becomes $\|\overrightarrow{u}\| = 38.32$ m/s. The cell size used in the simulations was 2 m.

The results of the simulation, obtained with TRENT2D$^\circledast$, are reported in Fig. 12, where the non-dimensional velocity $u_\pi^*(t^*)$, the non-dimensional vertical depth $h_v^*(t^*) = h_v/h_v^0$, and the respective relative errors, defined as:

$$
\begin{aligned}
E_u(t^*) &= \frac{\left[u_\pi^*(t^*) \right]^a - \left[u_\pi^*(t^*) \right]^n}{\left[u_\pi^*(t^*) \right]^a} \\
E_h(t^*) &= \frac{\left[h_v^*(t^*) \right]^a - \left[h_v^*(t^*) \right]^n}{\left[h_v^*(t^*) \right]^a}
\end{aligned}
\tag{88}
$$

where the superscripts a, n stand for analytical and numerical respectively, are plotted as a function of the non-dimensional time t^*. Errors have been evaluated considering four decimal places both for the analytical and for the numerical values. The plots show a good agreement between the numerical results and the analytical solutions. We tested different channel width (ranging from 10 up to 200 m) and no difference in the numerical results was observed. The relative errors are quite low for the velocity and essentially null for the depth. The reason for this latter feature is the fact that the channel walls are aligned with one reference axis and therefore the geometrical discretization error of

the boundaries is null. In these conditions, the numerical scheme can to compute exactly the effect of the wall (see Section 6.1.2).

Fig. 13 shows the results of the simulation obtained with RAMMS2D for a channel width of 200 m. In this case, errors are larger than the ones reported in Figs. 12 and they become quite large for $t^* > 3$ because of the spurious influence of the walls (see again Section 6.1.2) and, for this reason, they are not reported. Analogously, the velocity relative errors obtained in the initial phase of the motion are not reported because they fall outside the plot limits. With lower channel width the spurious influence of the walls becomes relevant for $t^* < 3$.

The obtained results clearly show the great accuracy of the overall numerical scheme proposed in this paper when applied to unsteady conditions.

6.2.3. Straight channel sloping in a direction rotated with respect to the axes

In this test, the channel direction π is rotated with respect to the horizontal reference axes. Because of the Cartesian discretization, in this case, the channel boundaries are not defined by a straight line but by a piecewise constant function. A boundary discretization error is expected to progressively affect the numerical solution from the boundaries to the middle of the channel. To obtain a centreline section unaffected by this phenomenon (at least for a certain time), the width was set equal to 100 m.

As for the other geometrical characteristics, the angles that the bed channel plane forms with the horizontal reference axes are $\alpha_x = \alpha_y = 20°$ while the angle of the bed normal is $\theta = 27.24°$.

The release prism is 458 m long in the π direction, has a width equal to the width of the channel, and its normal depth is $h^0 = 1.5$ m (to which corresponds a vertical depth $h_v^0 = 1.687$ m). The friction parameters have been set up like in the previous test. With this data, we obtain $t_a = 10.56$ s, $\|u_\pi^\infty\| = 25.762$ m/s and a velocity norm $\|\overrightarrow{u}\| = 28.974$ m/s. The cell size used in the simulations was 1 m.

The results of the simulation, obtained with TRENT2D$^\circledast$, are reported in Fig. 14, where the non-dimensional velocity $u_\pi^*(t^*)$, the vertical depth $h_v^*(t^*)$ and the respective relative errors are plotted as a function of the non-dimensional time t^*. Also in this test, the model reproduces well the analytical solution with small relative errors up to $t^* = 1$. After this time, the influence of the wall discretization affects the solution, and the errors increase but remain limited. These results confirm the quality of the
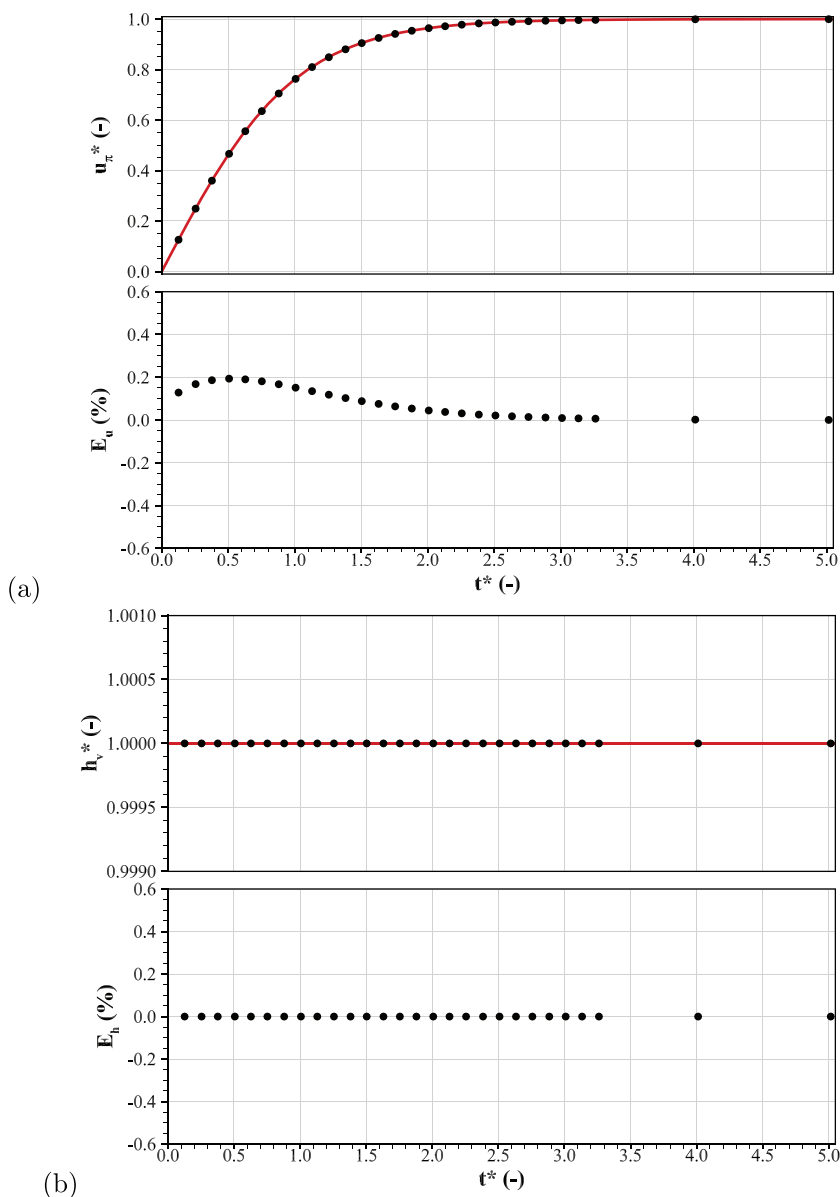
Fig. 12. TRENT2D* results concerning the straight channel test, sloping in the π direction aligned with the *y*-axis. (a) Non-dimensional velocity (top) and the respective relative error (bottom) and (b) non-dimensional flow depth (top) and the respective relative error (bottom) as a function of the non-dimensional time. In all the plots red lines indicate the analytical solutions while black dots represent the numerical results. (For interpretation of the references to colour in this figure legend, the reader is referred to the web version of this article.)

overall numerical scheme and the correct implementation of the scheme in the 2D case.

The results obtained with RAMMS2D are similar to the ones plotted in Fig. 13 but in this case, the relative errors are larger. For the sake of brevity, they have not been reported.

6.3. The truncated pyramid tests

The tests presented in this section are primarily designed to validate the algorithm for the static case with free-surface gradients (see Section 5.5). The initial condition for all the tests consists of a truncated snow pyramid positioned on a flat horizontal bed, with sides parallel to the horizontal reference axes as sketched in Fig. 15. The truncated pyramid has a square bottom base with sides 80 m long, the height of 5 m and the steepest slope of the sides is $i_\eta = 0.2$. The angle θ is identically zero.

As friction parameters, we chose $\xi = 1500$ m/s^2 while μ varies between tests. The computational domain was discretized with cells of side 1 m.

Case 1: $\mu > i_\eta$. In this case, the truncated pyramid is in conditions of stable equilibrium. For the test, we have set $\mu = 0.25$. Fig. 16(a) shows

that TRENT2D* numerical solution is, as expected, completely steady, while RAMMS2D results present a flow that continuously deforms the truncated pyramid.

Case 2: $\mu = i_\eta$. In this case, the truncated pyramid is in conditions of limiting equilibrium. For this reason, we can expect that the numerical approximation in the slope evaluation could lead to some areas having small movements. In this test $\mu = 0.2$. As shown in Fig. 16(b), the proposed model shows deformations that are limited to small portions of the section near the slope discontinuity located between the top line and the side line while, once again, the other model presents continuous deformations over time.

Case 3: $\mu < i_\eta$. In this case, the truncated pyramid is not in equilibrium but, because of the flat bed condition, a limited deformation is expected before an equilibrium condition is reached, characterized by the steepest slope equal to μ or slightly smaller near the front where the inertial terms reach larger values during the flow phase. Therefore, this test involves both the stopping algorithm and the static case with free surface gradients algorithm. In this case, we have set $\mu = 0.15$, Fig. 17 shows that with TRENT2D*, the no-motion condition is reached and maintained after 10 s and it is characterized, as expected, by a section
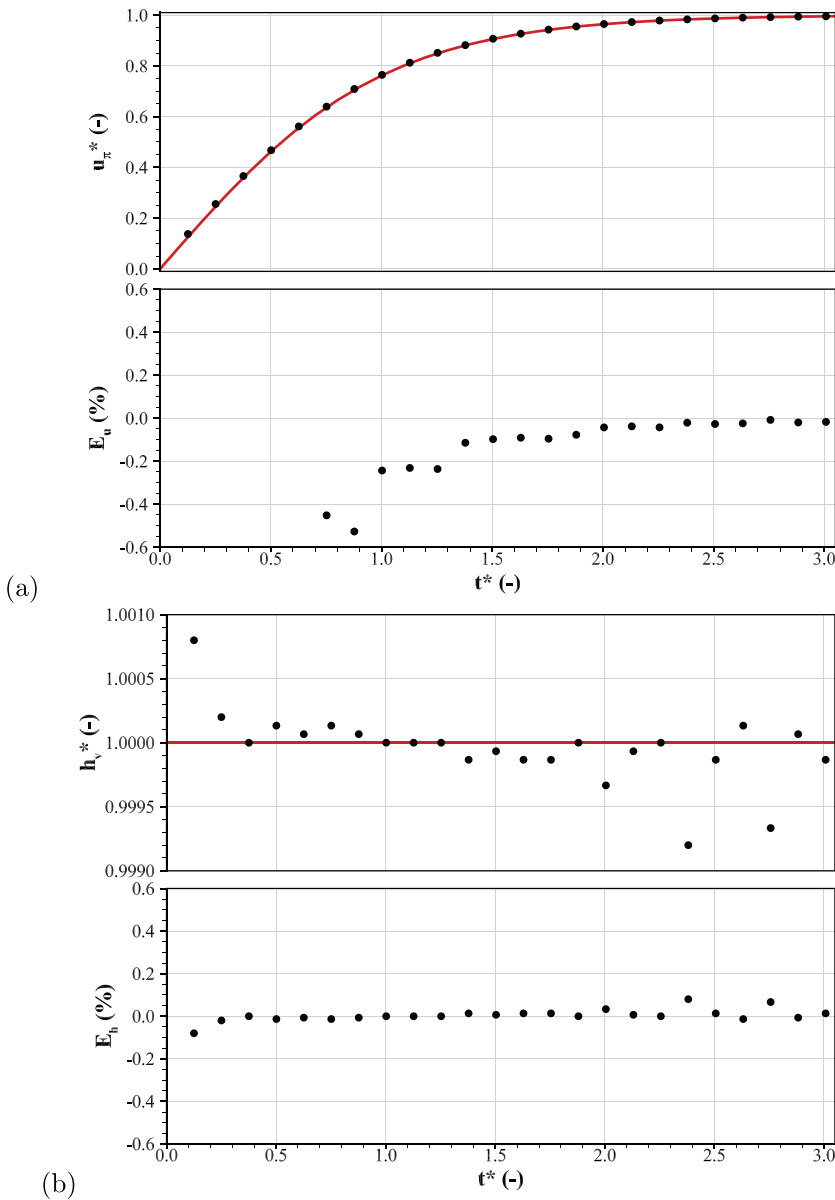
Fig. 13. RAMMS2D results concerning the straight channel test sloping in the π direction aligned with the y-axis. (a) Non-dimensional velocity (top) and the respective relative error (bottom) and (b) non-dimensional flow depth (top) and the respective relative error (bottom) as a function of the non-dimensional time. In all the plots red lines indicate the analytical solutions while black dots represent the numerical results. (For interpretation of the references to colour in this figure legend, the reader is referred to the web version of this article.)

with a decreasing slope from the middle to the front. RAMMS2D shows a solution that resembles the one obtained with our model (except in the middle) up to the time of 10 s. However, differently from our solution, after that time the flow goes on endlessly.

The truncated pyramid tests assesses the capability of TRENT2D* to deal correctly with the static case with free surface gradients and with the complete stopping of a flow on a horizontal flat bed. Moreover, no numerical instability arises in the centre of the pyramid as it happens in all the simulations performed with RAMMS2D.

6.4. Tests with stopping on an inclined flat bed

This set of test cases is mainly intended for the assessment of the stopping algorithm presented in Section 5.4. Nevertheless, as highlighted in Case 3 of the truncated pyramid test, also the algorithm for the static case with free-surface gradients is involved since, once the flow has stopped, the no-motion condition must be maintained. To minimize the possible effects related to the curvature of the bed surface (negligible, according to the basic assumptions), the slope changes quite smoothly. In particular, the terrain is composed of four different planes

with zero slope in the y-direction and constant slope in the x-direction. The steepest slope decreases by 1° passing from one plane to another, starting from a slope of 15° in the upper plane. The longitudinal bed section of this system and the release prism are sketched in Fig. 18. The total horizontal length of the system is 1200 m, the horizontal lengths of the planes, starting from the uppermost one, are 400 m, 24 m, 24 m and 752 m respectively while the horizontal length of the release prism is L_d = 180 m.

Two different tests with this bed configuration have been considered: a flow in a straight 1D channel with direction aligned with the steepest-slope direction and a completely unconfined, fully 2D flow. In both cases, the μ parameter was chosen in such a way as to cause the avalanche to stop mainly in the lower plane. As already highlighted in the Case 3 of the truncated pyramid test, thanks to the algorithm present in the TRENT2D* model, once an avalanche stops at a given time, it no longer moves even if the numerical simulation continues. This does not occur in RAMMS2D, where the flow either does not stop or stops and then moves again. To overcome this drawback, RAMMS2D implements the following stopping criterion in the numerical algorithm: when the ratio of the global momentum of the snow at the n-th time-step divided
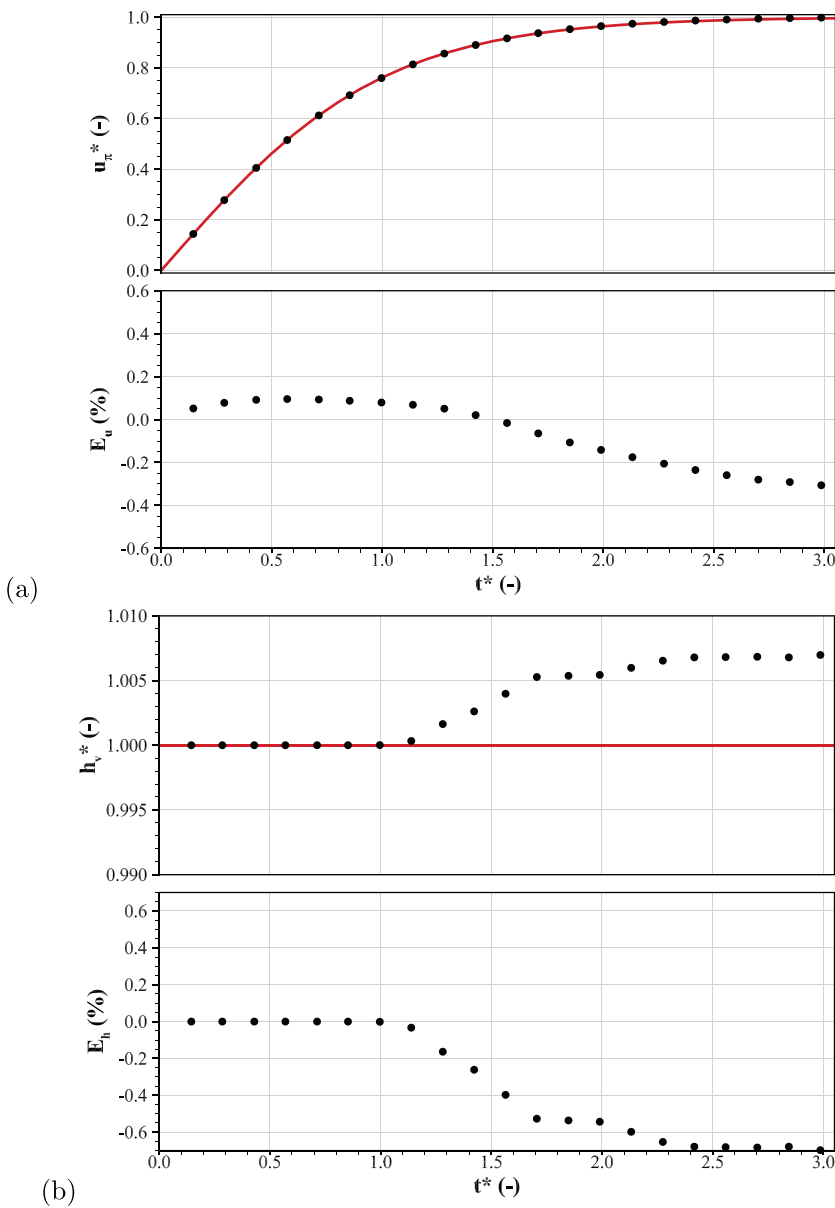
Fig. 14. TRENT2D* results concerning the straight channel test sloping in the π direction rotated with respect to the axes. (a) Non-dimensional velocity (top) and the respective relative error (bottom) and (b) non-dimensional flow depth (top) and the respective relative error (bottom) as a function of the non-dimensional time. In all the plots red lines indicate the analytical solutions while black dots represent the numerical results. (For interpretation of the references to colour in this figure legend, the reader is referred to the web version of this article.)
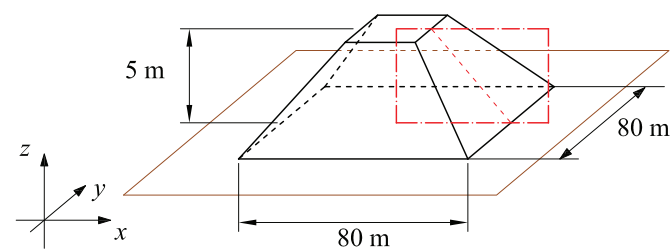
Fig. 15. Geometric characterization of the truncated snow pyramid at rest. The red dot-dashed rectangle indicates the section where the simulation results are analysed and plotted in Figs. 16 and 17. (For interpretation of the references to colour in this figure legend, the reader is referred to the web version of this article.)

by the maximum momentum achieved during the simulation up to that time is lower than a threshold defined by the user, then the simulation ends regardless of the speeds still present. Mathematically, the momentum ratio can be expressed as:

$$K_R(n) = \frac{\sum_{i,j} h_{i,j}^n \left| U_{i,j} \right|^n}{max\left(\sum_{i,j} h_{i,j}^t \left| U_{i,j} \right|^t ; \ t = 1, \ldots, n \right)} \tag{89}$$

where the sum is over all the cells. No clear justification for this criterion is available, but the manual recommends threshold values in the range $1\% \leq K_R \leq 10\%$. It is worth noting that this stopping criterion is equivalent to introducing one more parameter in the Voellmy friction law.

The stopping of an avalanche can be characterized by identifying the runout distance, the shape of the front (in plan and section) and the time when the front (or most of the avalanche) stops. For the two tests described above, no analytical solution is available and therefore, only the comparison between the two models can be analysed. Because of the different stopping algorithms employed, as reference stopping time we used the time when the front stops definitively in the lower plane, indicated with the symbol t_{stop}, for the TRENT2D* results while we used the simulation ending time, indicate with the symbol t_{end}, for the RAMMS2D results. This last quantity depends on the threshold value chosen for K_R.
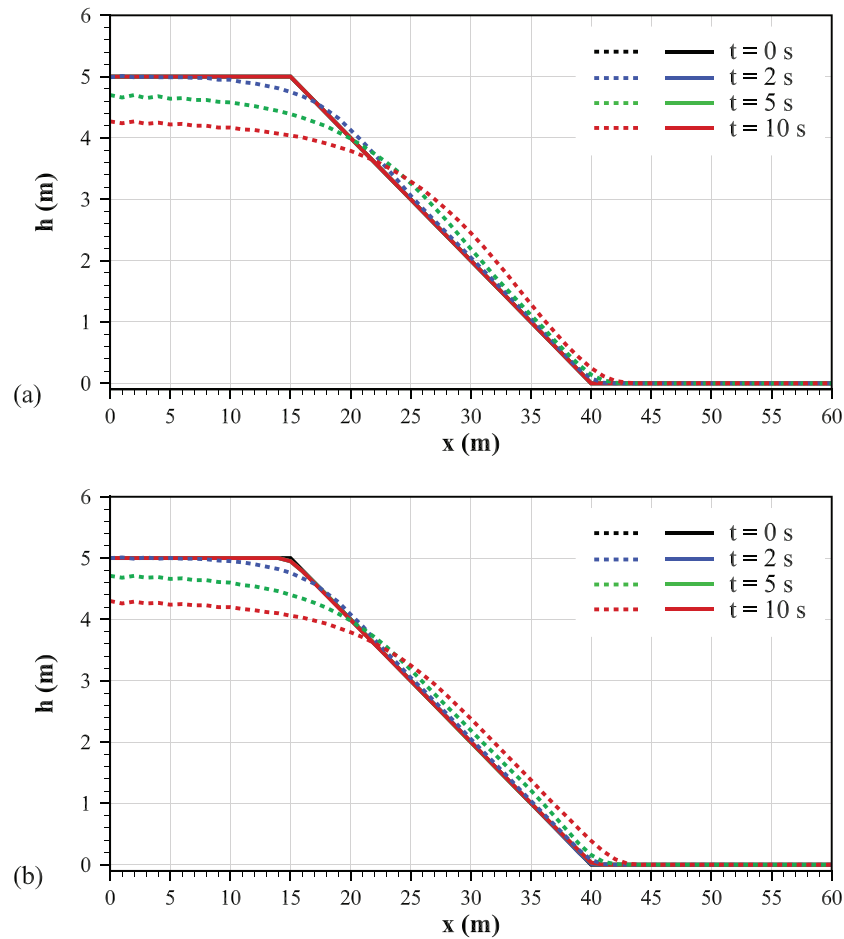
Fig. 16. Normal depth of a half mid-section of the truncated pyramid test; (a) case with $\mu = 0.25 > i_\eta$; (b) case with $\mu = 0.20 = i_\eta$. In all the plots, TRENT2D$^{\circledast}$ outputs are drawn with solid lines while RAMMS2D outputs are drawn with dashed lines.

6.4.1. Straight channel with decreasing slope bed

In this test, the channel direction π is aligned with the x-direction and the bed slope decreases in the flow direction as described previously. The release prism has a width equal to the channel width (198 m) and its normal depth is $h^0 = 1$ m (to which corresponds a vertical depth $h_v^0 = 1.035$ m). Friction parameters are: $\mu = 0.23$, (to which corresponds an equilibrium free-surface slope angle equal to 12.95°), and $\xi = 2000$ m/s^2. The flow domain has been discretized with cells of side equal to 2 m.

In Fig. 19, the trend of the normal depth and the velocity vector norm obtained with TRENT2D$^{\circledast}$ and with RAMMS2D is plotted, for a longitudinal section, as a function of the horizontal distance from the beginning of the channel. Reference stopping times are $t_{stop} = 108$ s and $t_{end} = 87$ s, 97 s, 175 s corresponding to values of K_R equal to 10%, 5% and 1% respectively.

The shape of the avalanche and the velocity distributions in the tail differs significantly from one simulation to the other because they are evaluated at different times.

In the lower plane, the shape of the TRENT2D$^{\circledast}$ section is similar to the sections obtained with RAMMS2D with $K_R = 5\%$ and $K_R = 10\%$ but, in these cases, significant velocities are still present in the snow. On the contrary, velocities are almost null in the RAMMS2D results with $K_R = 1\%$ as in the TRENT2D$^{\circledast}$ results but in this case, the shape of the section is quite different and wiggles in the velocities appear.

The details of the fronts at the reference stopping times are plotted in Fig. 20 and the corresponding runout distances R_d are listed in Table 1 for all the simulations. Results show that the differences between the two models in terms of runout distances are limited but, considering the shape of the front and mainly the residual velocities, the differences in

terms of impact pressures are more significant. Finally, while for TRENT2D$^{\circledast}$ the runout distance and the stopping time are quantities that, given a flow geometry and given initial conditions, depend only on μ and ξ, in RAMMS2D these quantities depend, as expected, not only on the Voellmy parameters but also on the K_R parameter. For this test case, the K_R parameter that produces results that come closest to the proposed model is 5% (the default value for the model). Nevertheless, this last result is not general, as will appear in the following test.

6.4.2. Unconfined flow over decreasing slope bed

In this test the release prism is located in the same position as in the previous case, is 50 m wide in the y-axis direction and its normal depth is $h^0 = 3$ m (to which corresponds a vertical depth $h_v^0 = 3.106$ m). Friction parameters are: $\mu = 0.225$ (to which corresponds an equilibrium free-surface slope angle equal to 12.68°), and $\xi = 2500$ m/s^2. As previously, the cell size is 2 m.

In Fig. 21, the trend of the normal depth obtained with TRENT2D$^{\circledast}$ and RAMMS2D is plotted as a function of the horizontal distance from the beginning of the channel for a middle longitudinal section. In Table 2, the corresponding runout distances are listed. Unlike the previous test, the case with $K_R = 1\%$ is missing because, with this value, the flow does not stop within the end of the lower plane and therefore has not been reported. Reference stopping times are $t_{stop} = 134$ s and $t_{end} = 86$ s, 94 s corresponding to values of K_R equal to 10%, 5% respectively.

In this test, the differences between the results of the two models are more marked than in the previous test:
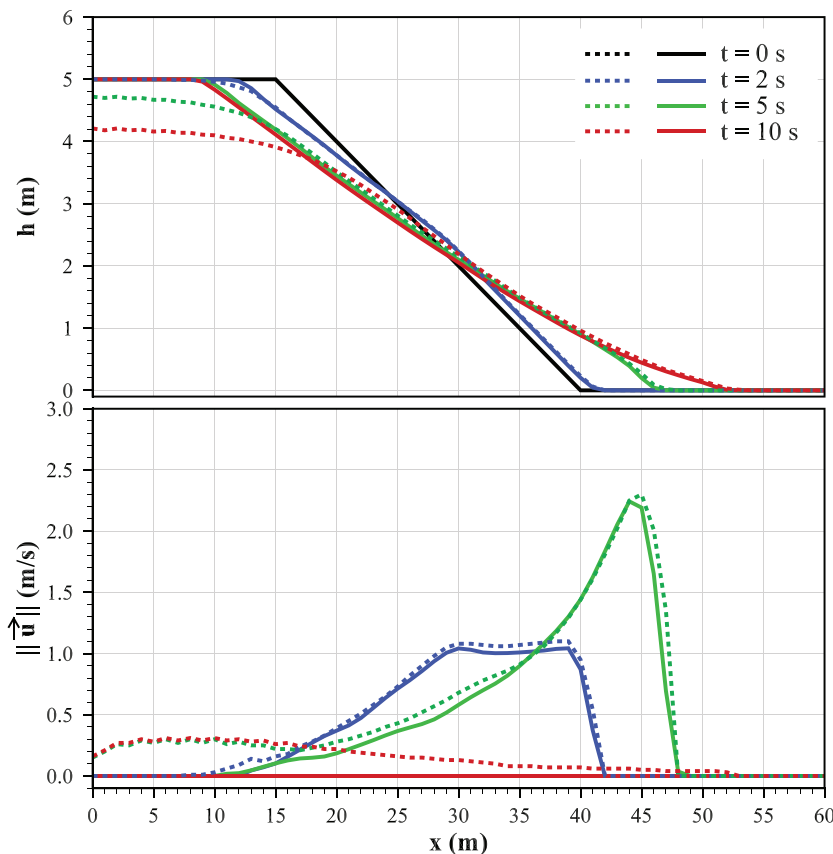
Fig. 17. Normal depth (top) and velocity (bottom) of a half mid-section of the truncated pyramid test with $\mu = 0.15 < i_\eta$. In all the plots, TRENT2D* outputs are drawn with solid lines while RAMMS2D outputs are drawn with dashed lines.
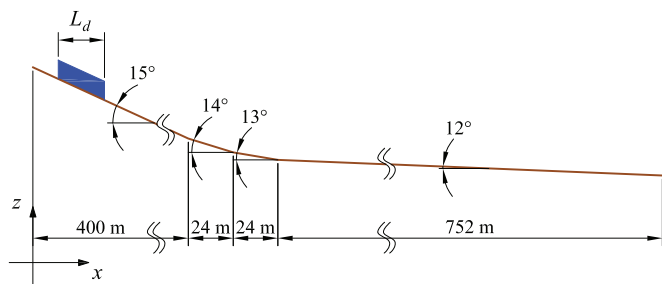

Fig. 18. Longitudinal section and geometrical characteristics of the bed surface and the release prism used in the tests with stopping on an inclined flat bed.

- the runout distance obtained with our model is larger and differs by 24 m and 38 m from the distances obtained with the other model with different K_R values;
- significant differences can be noticed in the shape of the deposits in the front and the tail of the middle longitudinal section (Fig. 21);
- the solution obtained with $K_R = 5\%$ does not give a matching in the runout distance between the two models, as happened in the previous test (Fig. 21);
- the maximum planimetric extension reached by the snow depth during the whole simulation obtained with the proposed model (Fig. 22) shows two side expansion near the last change of slope that is absent in the results of RAMMS2D;
- while the velocity norms obtained with our model are null in the lower plane area, the results of the other model present large areas near the front with velocity norms up to 2 m/s (Fig. 22).

The reason for these differences can be partially justified considering

that the times at which the solutions are considered are different. In the TRENT2D* case, the pile of snow in the lower plane begin to stop around $t = 120$ s while the front and the tail keep on moving. The front stops completely at t_{stop} while the snow of the tail is still moving. This explains the snow accumulation in the back of the lower plane pile (410 m $\leq x \leq$ 470 m in Fig. 21) and the lateral expansions. This behaviour is not present in the RAMMS2D simulations because, in these cases, at the actual simulation ending times the front pile is not steady and significant velocities are still present. This explains why the front is not completely developed and the snow in the back of the lower plane pile does not accumulate.

Lacking a reference solution, we can only state that compared to the results obtained with RAMMS2D, the TRENT2D* results seem more reasonable in terms of velocity distribution at the reference time and less uncertain since, once again, they depend only on the Voellmy friction parameters.

6.5. Flow with submersible retarding structures

This test is designed to assess the ability of TRENT2D* to cope with bed steps that can be submerged during the flow. It consists of releasing a prism of snow over a decreasing slope bed as in the test presented in Section 6.4.2 but this time a series of retarding structures have been inserted in the upper plane near the first decrease of slope (see Fig. 23). The shape, distribution and height of these structures have been chosen in such a way as to induce a rather complex avalanche dynamics in which all possible flow conditions over bed steps occur. Efficiency to reduce the runout distance was not considered.

Results concerning the vertical heights are reported in Fig. 24 for two different times while in Fig. 25 zooms of these results near the central retarding structure are plotted together with the related velocity vector
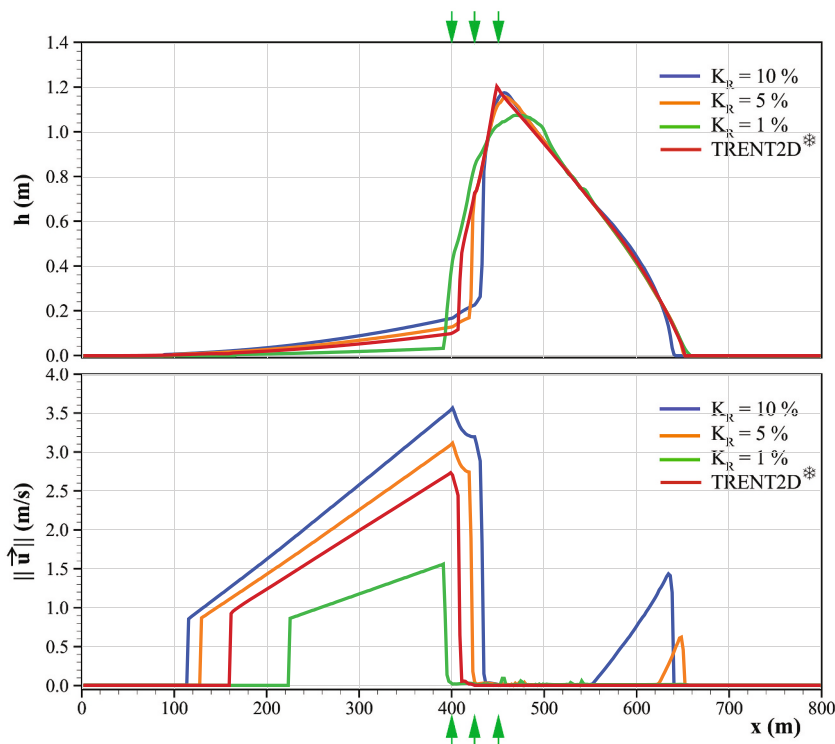
Fig. 19. Normal depth (top) and velocity norm (bottom) along a longitudinal section of the straight channel with decreasing slope bed test at the stopping reference times (see text for their definitions). The green arrows indicate the points where the slope of the bed changes. (For interpretation of the references to colour in this figure legend, the reader is referred to the web version of this article.)
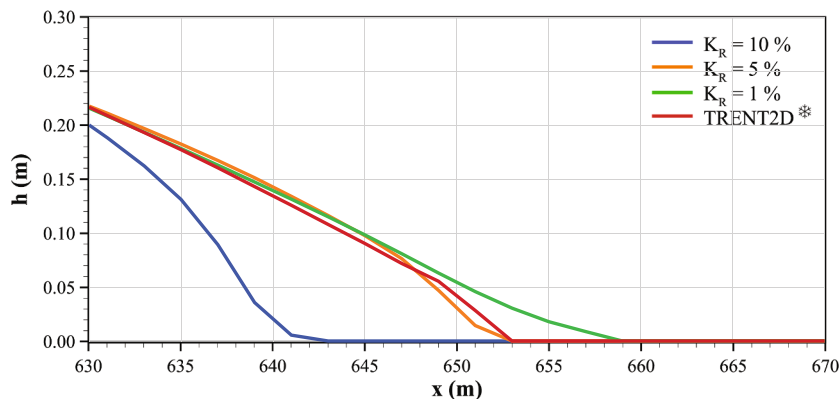

Fig. 20. Details of the flow depth h near the front of the avalanche for the decreasing slope bed test at the stopping reference times obtained with TRENT2D* and RAMMS2D for different values of K_R.

Table 1
Runout distance R_d for the straight channel with decreasing slope bed test evaluated at the stopping reference times (t_{ref}) for the TRENT2D* and RAMMS2D models.

	TRENT2D*	RAMMS2D		
K_R	–	10%	5%	1%
t_{ref} (s)	108	87	97	175
R_d (m)	651	641	651	657

fields. The first time is relative to when the avalanche front impacts on the first row of structures generating inclined shocks increasing the vertical heights and reducing the velocities in front of the structures; the second time is relative to when the flow has overtopped both rows of structures.

Since an analytical solution is not available, we can only notice that from a numeric point of view the flow is symmetric, does not present instabilities and the distributions of heights and velocity vectors are completely reasonable. From a physical point of view, we are not able to assess the reliability of the results in comparison with the reality, but this topic is actually outside the scope of the paper. In any case, the effect of the retarding structures can be appreciated by comparing the map of the vertical height obtained in the test presented in the previous section with the results of the present test at the same time $t = 134$ s (namely the t_{stop} of the previous test). As can be noticed in Fig. 26, the runout distance, evaluated after full stop, is decreased by about 50 m, the maximum width is increased by about 20 m and the snow pile is more developed around the last slope change.
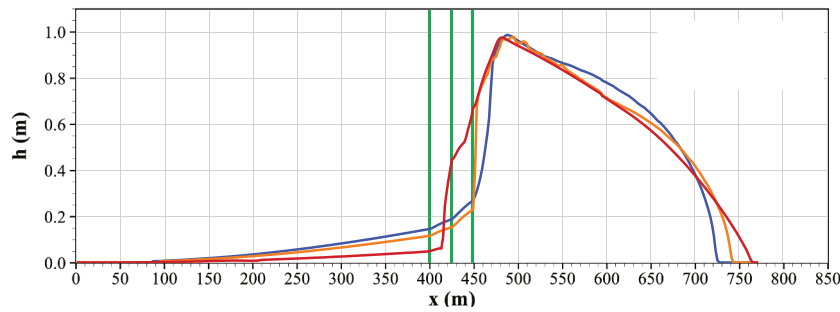
Fig. 21. Normal depth as a function of the horizontal distance from the beginning of the channel for a middle longitudinal section of the unconfined flow over decreasing slope bed test at the stopping reference times (see text for their definitions). The green vertical lines indicate the points where the slope of the bed changes. (For interpretation of the references to colour in this figure legend, the reader is referred to the web version of this article.)

Table 2
Runout distance R_d for the unconfined flow over decreasing bed slope test evaluated at the reference time (t_{ref}) for the TRENT2D$^❅$ and RAMMS2D models.

	TRENT2D$^❅$	RAMMS2D	
K_R	–	10%	5%
t_{ref} (s)	134	86	94
R_d (m)	766	728	744

7. Conclusions

The goal of the work presented in this paper was to develop a new mathematical and numerical approach, able to accurately simulate two-dimensional, dense snow avalanches described as a single-phase, shallow fluid with a Voellmy friction law. The novelties we introduced consist of the use of the flow equations written in a global coordinate system and the development of specific algorithms for the treatment of the effects of the velocity-independent term in the Voellmy friction law,

namely the stopping of a flow and the maintenance of steady conditions with inclined free surfaces. Added to the use of a well-balanced, finite volume numerical approach, already employed by the authors in debris-flow modelling, these novelties allow the resulting numerical model to deal with almost all the situations that an avalanche may encounter: flows bounded by vertical and emerging walls, any sort of steady conditions, flow stops and submerged bed steps.

The results of the tests performed, specially developed to assess the model capabilities, confirm that the objective has been achieved:

- no spurious movement is generated starting from steady conditions with both horizontal and inclined free surfaces;
- uniform accelerating flows are well reproduced in comparison with the analytical solution in any direction of the space;
- the stopping point of a flow depends only on the values of the friction parameters;
- instabilities appeared neither in any of the simulations performed nor in other test cases not reported in this paper.
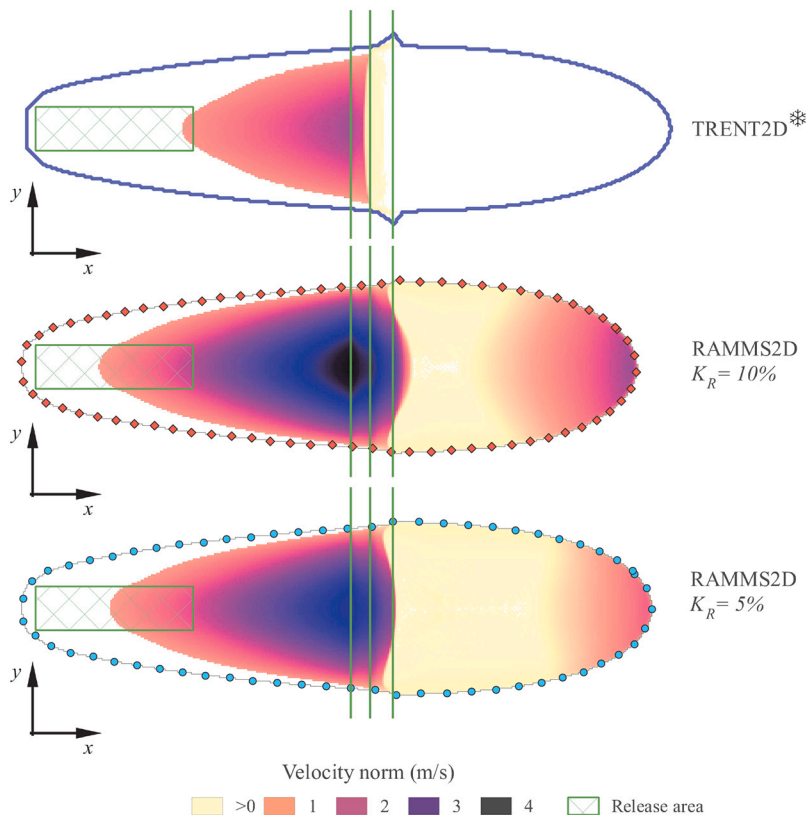

Fig. 22. Maximum planimetric extension reached by the snow depth during the whole simulation (outer lines) and maps of the velocity vector norm evaluated at t_{ref} obtained with the TRENT2D$^❅$ and RAMMS2D simulations of the unconfined flow over decreasing slope bed test. The green rectangle represents the release zone, while green lines are located where the bed slope changes. Only velocities associated with a normal flow depth greater than 0.01 m are plotted. (For interpretation of the references to colour in this figure legend, the reader is referred to the web version of this article.)
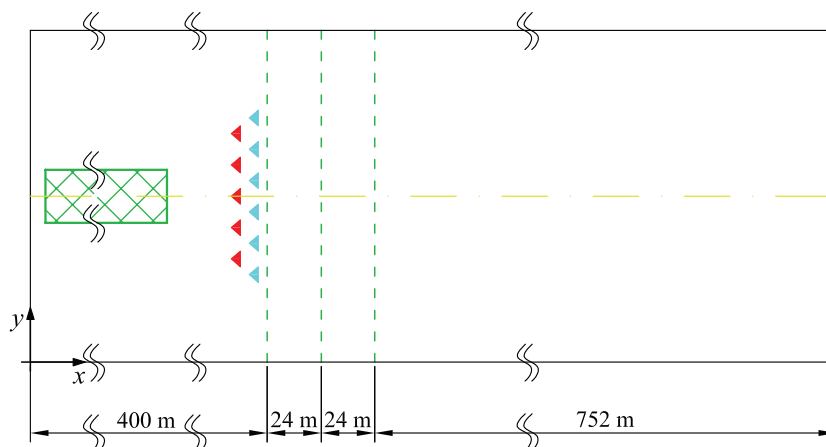
Fig. 23. Top view of the bed configuration used for the submersible retarding structures test. The green box indicates the release prism while triangles represent the retarding structures, the red ones are 3 m high, the cyan ones are 1 m high. Longitudinal section without structures as in Fig. 18. (For interpretation of the references to colour in this figure legend, the reader is referred to the web version of this article.)
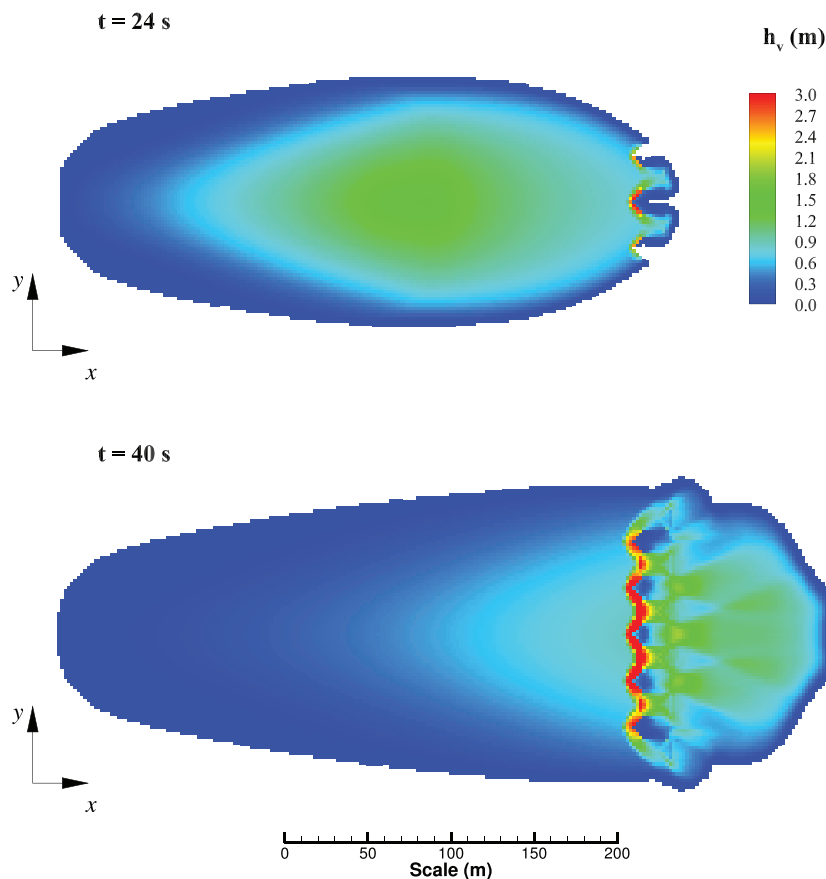

Fig. 24. Vertical height maps for the submersible retarding structures test at two different times.

The achieved accuracy of the numerical scheme is important for, at least, the following three reasons: (a) it makes the calibration of the proposed model less uncertain compared to other models since the actual number of parameters is equal to the number of parameters expected theoretically; (b) possible differences in the model results compared to laboratory or field data can be charged primarily to limits of the employed physical model and not to the numerical limits; (c) a more accurate numerical model means more reliable hazard maps and hazard assessments, provided that the Voellmy fluid model is the right avalanche description.

What we have proposed in this paper must be seen as a first, promising step towards the development of an effective tool for practical applications. Our future work will focus on making improvements to many aspects, some of which are more easily accomplished while others require more effort. A first improvement regards the ease of use of the model. Here we can exploit the capabilities of the WEEZARD system (Rosatti et al., 2018) that, thanks to its modular structure, allows one to include different types of models in a single web-service, GIS environment (available at http://tool.weezard.eu). In this way, a multi-purpose, multi-risk analysis tool for mountain regions can be easily obtained.
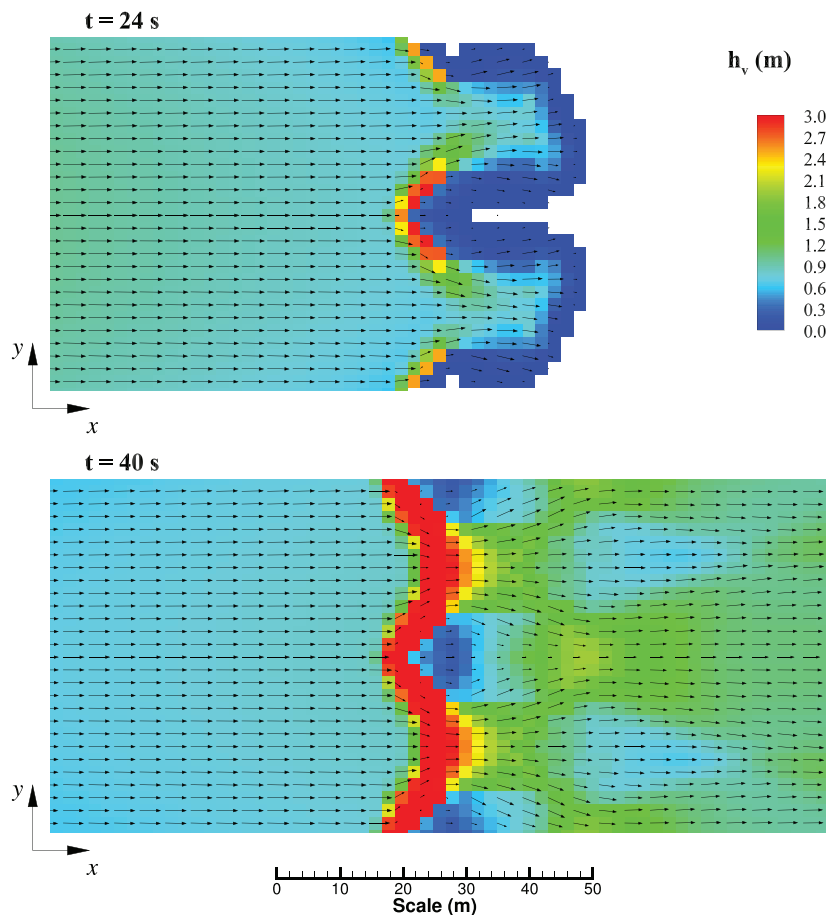
Fig. 25. Detail of the vertical height and velocity vector maps near the central retarding structure for the submersible retarding structures test at two different times.
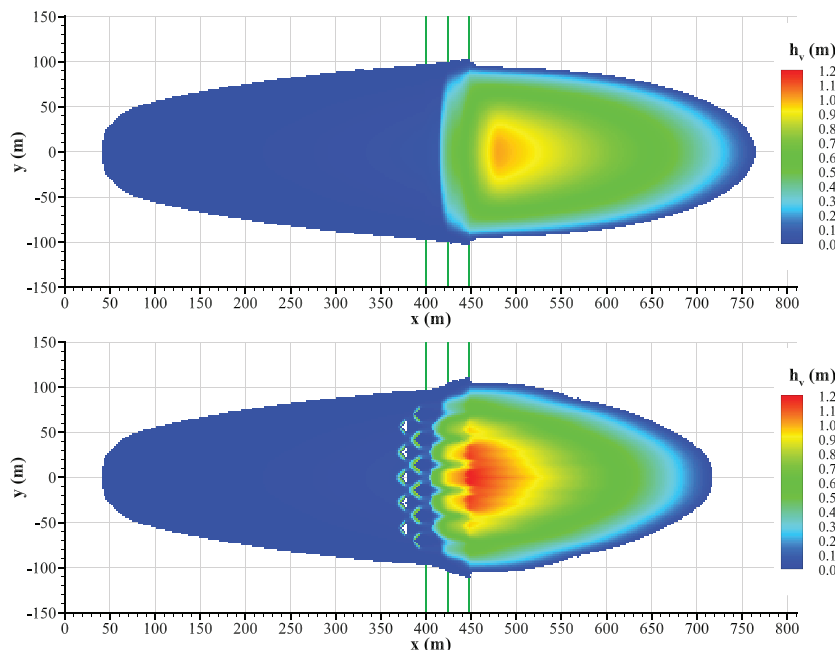

Fig. 26. Maps of vertical height distributions after full stop obtained (top) without retarding structures and (bottom) with retarding structures.

Another feature, quite easy to get, concerns the use of an unstructured grid. The employed numerical strategy adapts without any particular problem to this kind of domain discretization. However, developing a reliable and easy-to-use grid generator is not quite as easy.

Some other improvements may regard more specifically the mathematical model. Besides the classical Voellmy relation, other friction laws present in the literature (see the cited papers in the Introduction) can be employed in the model. From a numerical point of view, this means that

the algorithm used to retrieve the primitive variables from the conserved ones must be adequately (and perhaps easily) adapted. Other aspects may concern the relaxation of some hypotheses, as the small curvature, the hydrostatic assumption and the incompressibility condition, or the introduction of a suitable description of the entrainment process. Last but not least, model validation against experimental data is desirable.

All of these points are challenging and need to be resolved to arrive at accurate avalanche modelling.

Author statement

Daniel Zugliani and Giorgio Rosatti equally contribute to all the phases of the manuscript.

Declaration of Competing Interest

None.

Appendix A. Estimate of the velocity profile factor $\alpha_{u_x^2}$

In the present Appendix, we provide a demonstration that, under reasonable conditions, the corrective coefficient $\alpha_{u_x^2}$ can be assumed unitary.

Let us consider an instantaneous 1D flow as in Fig. A.27. To simplify the notation, in the following we do not indicate the time dependency of the variables. Let us place the origin of the LCS in such a way that the ζ-axis intersects the free surface at the same point where the vertical section, in which we want to evaluate the corrective coefficient α_{ux}^2, intersects the free surface. According to the Voellmy-fluid assumptions (see Section 2.2), the distribution of the velocity parallel to the bed can be written in the following way:

$$U(\chi) = U_0 f(\chi)$$

where $f(\chi)$ is a given nondimensional function describing the longitudinal variability of the velocity. We then assume that this function is linear, spanning from the unitary value in the origin of the χ-axis, to the null value at a distance that is a multiple of the flow depth h. Therefore, the distribution becomes:

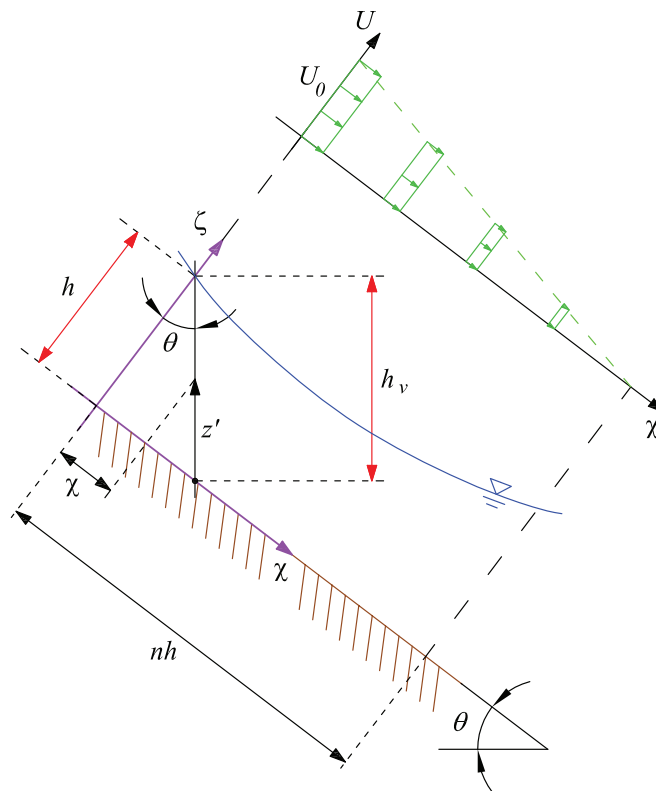$$U(\chi) = U_0 \left(1 - \frac{\chi}{nh}\right)$$

Fig. A.27. Scheme for the evaluation of the corrective coefficient along the vertical direction.

Introducing the variable $z' = z - z_b$, then $\chi = (h_v - z') \sin \theta$. Considering that $h = h_v \cos \theta$ and assuming $\theta = const$ in the χ-interval $[0, h_v \sin \theta]$, then the x-component of the velocity along the z'-coordinate becomes:

$$u_x'(z') = U(\chi)cos\theta = U_0\left(1 - \left(1 - \frac{z'}{h_v}\right)\frac{1}{n}\frac{sin\theta}{cos\theta}\right)cos\theta$$

The relevant depth-averaged velocity becomes:

$$u_x = \frac{1}{h_v}\int_0^{h_v} U_0\left(1 - \left(1 - \frac{z'}{h_v}\right)\frac{1}{n}\frac{sin\theta}{cos\theta}\right)cos\theta\, dz' = U_0\frac{1}{2n}(2ncos\theta - sin\theta)$$

while the depth-averaged value of $\left(u_x'\right)^2$ becomes:

$$\overline{u_x^2} = \frac{1}{h_v}\int_0^{h_v} U_0^2\left(1 - \left(1 - \frac{z}{h_v}\right)\frac{1}{n}\frac{sin\theta}{cos\theta}\right)^2 cos^2\theta\, dz' = U_0^2\frac{1 + 3n^2 - cos2\theta + 3n^2cos2\theta - 3nsin2\theta}{6n^2}$$

and finally, the velocity distribution factor becomes:

$$\alpha_{u_x^2}(\theta, n) = \frac{\overline{u_x^2}}{(u_x)^2} = \frac{2}{3}\frac{3n^2cos2\theta - cos2\theta - 3nsin2\theta + 3n^2 + 1}{(sin\theta - 2ncos\theta)^2}$$

In Fig. A.28, we plotted the value of the previous function for $n = 2,5,10,100$ and $0 \leq \theta \leq 90°$. The grey area in the diagram, spanning from 25° to 60°, represents what is commonly referred to as the range of slopes within which avalanches are triggered.
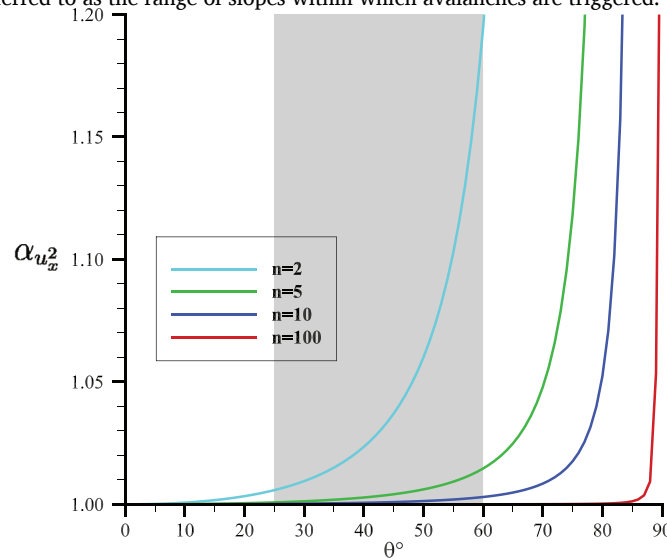

Fig. A.28. Plot of $\alpha_{u_x^2}$ as a function of the bed slope for different values of the parameter n.

The following consideration can be done:

- For a smooth variation of the velocity profile, condition represented by the curve with $n = 100$, the coefficient can be considered unitary for all the slopes except for 90°, where the step condition can be applied.
- For sharp variations, condition represented by the curves with $n = 2, 5$, the coefficient is almost unitary up to values of $\theta = 60°$, where the values of 1.1944 and 1.0146 are reached respectively. Therefore, for sharp variations occurring in the stopping zone, the coefficient is essentially unitary while can become greater that one in case of sharp variations on a steep slope. This last condition could affect the speed of the avalanche front, but we think that this factor is negligible compared to the uncertainty of knowledge of the other parameters affecting the front speed.

In conclusion, we believe that this analysis strongly supports, even if it does not unequivocally prove it, the fact that the value for α_{ux}^2 is negligibly different from one in every practical situation.

Appendix B. Definition and characteristics of the tangent plane to a surface in a point

Given a bed surface as defined in Section 4 and its normal unit vector as defined in Eq. (48), in this section we derive and analyse the tangent plane $\mathscr{T}$ to the surface in the point where the surface intersects the z-axis, namely $\mathscr{P}_0 = (0, 0, z_0)$. However, results can be easily extended to any point of the bed surface.

Given a generic point $\mathscr{P} = (x, y, z)$, the vector joining this point to the reference point can be expressed as $\overrightarrow{T} = \mathscr{P} - \mathscr{P}_0 = (x, y, z - z_0)$. This vector lies on the tangent plane if and only if it is orthogonal to $\hat{n}$, namely $\overrightarrow{T}\cdot\hat{n} = 0$. The relevant Cartesian expression reads:

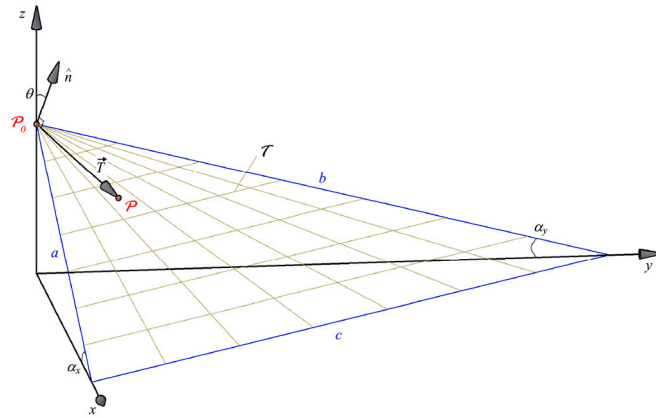$$n_x x + n_y y + n_z z = z_0 n_z \tag{B.1}$$

Fig. B.29. Sketch of plane $\mathcal{T}$ with relevant characteristics.

The intersection of $\mathcal{T}$ with the $x - z$ plane

$$z = -\frac{n_x}{n_z}x + z_0 \tag{B.2}$$

defines the straight line a of Fig. B.29 whose slope, by using Eq. (50) and introducing the angle α_x between a and the x-axis, can be expressed as:

$$-\frac{n_x}{n_z} = \frac{\partial z_b}{\partial x} = tan\alpha_x \tag{B.3}$$

Analogously, we define the straight line b as the intersection of $\mathcal{T}$ with the $y - z$ plane and, denoting by α_y the angle between b and the y-axis, its slope becomes:

$$-\frac{n_y}{n_z} = \frac{\partial z_b}{\partial y} = tan\alpha_y \tag{B.4}$$

With Eqs. (B.3) and (B.4), the quantity $cos\theta$ defined in Eq. (49) can be expressed as:

$$cos\theta = \frac{1}{\sqrt{1 + \left(tan\alpha_x\right)^2 + \left(tan\alpha_y\right)^2}} \tag{B.5}$$
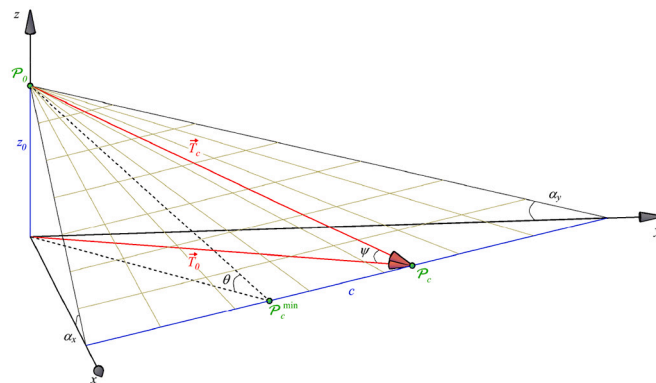

Fig. B.30. Points and vectors used in the determination of the maximum slope of $\mathcal{T}$.

The steepest slope of the plane can be obtained as follows. Let us consider the straight line c (Fig. B.29) deriving from the intersection of the plane $\mathcal{T}$ with the $x - y$ plane:

$$y = -\frac{n_x}{n_y}x + \frac{n_z}{n_y}z_0 \tag{B.6}$$

Let

$$\mathcal{P}_c(x) = \left(x, -\frac{n_x}{n_y}x + \frac{n_z}{n_y}z_0, 0 \right)$$

be a point lying on c, then we can define the following vectors:

1. $\vec{T}_c(x) = \mathscr{P}_c - \mathscr{P}_0$: a vector lying on $\mathscr{T}$;
2. $\vec{T}_0(x) = \mathscr{P}_c - (0, 0, 0)$: a vector lying on the plane $x - y$.

The cosine and the tangent of the angle ψ between the two vectors are:

$$cos\psi = \frac{\left\| \vec{T}_c \right\|}{\left\| \vec{T}_h \right\|}; \quad tan\psi = \frac{z_0}{\left\| \vec{T}_h \right\|} \tag{B.7}$$

The steepest slope of $\mathscr{T}$ is obtained when $tan\psi$ reaches its maximum value. Considering the previous equation, this condition becomes:

$$\frac{d}{dx} \left\| \vec{T}_h \right\| = 0 \tag{B.8}$$

The solution gives:

$$x_{\min} = -\frac{n_x n_z}{n_x^2 + n_y^2} z_0 \tag{B.9}$$

that is the x-coordinate of point $\mathscr{P}_c^{\min}$ (see Fig. B.30). Introducing this last expression into the first element of Eq. (B.7), we obtain the cosine of the maximum value of the slope

$$cos\psi = \frac{1}{n_z} = cos\theta \tag{B.10}$$

This result shows that the angle corresponding to the maximum slope of $\mathscr{T}$ is equal to the angle that the normal vector forms with the z- axis.

References

Armanini, A., Fraccarollo, L., Rosatti, G., 2009. Two-dimensional simulation of debris flows in erodible channels. Comput. Geosci. 35, 993–1006. https://doi.org/10.1016/j.cageo.2007.11.008.

Barbolini, M., Gruber, U., Keylock, C.J., Naaim, M., Savi, F., 2000. Application of statistical and hydraulic-continuum dense-snow avalanche models to five real European sites. Cold Reg. Sci. Technol. 31, 133–149. https://doi.org/10.1016/s0165-232x(00)00008-2.

Bartelt, P., Salm, B., Gruber, U., 1999. Calculating dense-snow avalanche runout using a Voellmy-fluid model with active/passive longitudinal straining. J. Glaciol. 45, 242–254. https://doi.org/10.3189/S002214300000174X.

Bouchut, F., Westdickenberg, M., 2004. Gravity driven shallow water models for arbitrary topography. Commun. Math. Sci. 2, 359–389. URL: https://projecteuclid.org:443/euclid.cms/1109868726.

Bouchut, F., Mangeney-Castelnau, A., Perthame, B., Vilotte, J.P., 2003. A new model of Saint Venant and Savage-Hutter type for gravity driven shallow water flows. Comp. Rend. Math. 336, 531–536. https://doi.org/10.1016/s1631-073x(03)00117-1.

Butler, D.R., Malanson, G.P., 1985. A reconstruction of snow-avalanche characteristics in Montana, U.S.A., using vegetative indicators. J. Glaciol. 31, 185–187. https://doi.org/10.3189/S0022143000006444.

Christen, M., Bartelt, P., Kowalski, J., Stoffel, L., 2008. Calculation of dense snow avalanches in three-dimensional terrain with the numerical simulation program RAMMS. In: Proceedings Whistler 2008 International Snow Science Workshop September 21-27, 2008, pp. 709–716. URL: https://arc.lib.montana.edu/snow-science/item/119.

Christen, M., Kowalski, J., Bartelt, P., 2010. RAMMS: Numerical simulation of dense snow avalanches in three-dimensional terrain. Cold Reg. Sci. Technol. 63, 1–14. https://doi.org/10.1016/j.coldregions.2010.04.005.

Dumbser, M., Toro, E.F., 2011a. On universal Osher type schemes for general nonlinear hyperbolic conservation laws. Commun. Comput. Phys. 10, 635–671. https://doi.org/10.4208/cicp.170610.021210a.

Dumbser, M., Toro, E.F., 2011b. A simple extension of the Osher Riemann solver to non-conservative hyperbolic systems. J. Sci. Comput. 48, 70–88. https://doi.org/10.1007/s10915-010-9400-3.

Eglit, M., Yakubenko, A., Zayko, J., 2020. A review of Russian snow Avalanche Models - from analytical solutions to novel 3D models. Geosciences 10, 77. https://doi.org/10.3390/geosciences10020077.

Gerbeau, J.F., Perthame, B., 2001. Derivation of viscous Saint-Venant system for laminar shallow water; Numerical validation. Discret. Contin. Dyn. Syst. B 1, 89–102. https://doi.org/10.3934/dcdsb.2001.1.89.

Gray, J.M.N.T., Wieland, M., Hutter, K., 1999. Gravity-driven free surface flow of granular avalanches over complex basal topography. Proc. Royal Soc. Lond. A: Math. Phys. Eng. Sci. 455, 1841–1874. https://doi.org/10.1098/rspa.1999.0383.

Grigorian, S.S., Ostroumov, A.V., 2020. On a continuum model for Avalanche flow and its simplified variants. Geosciences 10, 35. https://doi.org/10.3390/geosciences10010035.

Issler, D., 2020. Comments on "On a continuum model for Avalanche flow and its simplified variants" by S. S. Grigorian and A. V. Ostroumov. Geosciences 10, 96. https://doi.org/10.3390/geosciences10030096.

Iverson, R.M., Denlinger, R.P., 2001. Flow of variably fluidized granular masses across three-dimensional terrain: 1. Coulomb mixture theory. J. Geophys. Res. Solid Earth 106, 537–552. https://doi.org/10.1029/2000JB900329.

Juez, C., Murillo, J.M., García-Navarro, P., 2013. 2D simulation of granular flow over irregular steep slopes using global and local coordinates. J. Comput. Phys. 255, 166–204. https://doi.org/10.1016/j.jcp.2013.08.002.

LeFloch, P.G., Thanh, M.D., 2007. The Riemann problem for the shallow water equations with discontinuous topography. Commun. Math. Sci. 5, 865–885. https://doi.org/10.4310/CMS.2007.v5.n4.a7.

Mangeney, A., Bouchut, F., Thomas, N., Vilotte, J.P., Bristeau, M.O., 2007. Numerical modeling of self-channeling granular flows and of their levee-channel deposits. J. Geophys. Res. 112 https://doi.org/10.1029/2006jf000469.

Mangeney-Castelnau, A., Vilotte, J.P., Bristeau, M.O., Perthame, B., Bouchut, F., Simeoni, C., Yerneni, S., 2003. Numerical modeling of avalanches based on Saint Venant equations using a kinetic scheme. J. Geophys. Res. Solid Earth 108. https://doi.org/10.1029/2002JB002024.

O'Brien, J.S., Julien, P.Y., Fullerton, W.T., 1993. Two-dimensional water flood and mudflow simulation. J. Hydraul. Eng. 119, 244–261. https://doi.org/10.1061/(ASCE)0733-9429(1993)119:2(244).

Parés, C., Pimentel, E., 2019. The Riemann problem for the shallow water equations with discontinuous topography: the wet-dry case. J. Comput. Phys. 378, 344–365. https://doi.org/10.1016/j.jcp.2018.11.019.

Peruzzetto, M., Mangeney, A., Bouchut, F., Grandjean, G., Levy, C., Thiery, Y., Lucas, A., 2020. Topography Curvature Effects in Thin-Layer Models for Gravity-Driven Flows without Bed Erosion. URL: https://hal.archives-ouvertes.fr/hal-03039631. working paper or preprint.

Pitman, E.B., Le, L., 2005. A two-fluid model for avalanche and debris flows. Philos. Trans. Royal Soc. Lond. A: Math. Phys. Eng. Sci. 363, 1573–1601. https://doi.org/10.1098/rsta.2005.1596.

RAMMS::Avalanche, 2021. https://ramms.slf.ch/ramms/.

Rosatti, G., Begnudelli, L., 2010. The Riemann problem for the one-dimensional, free-surface shallow water equations with a bed step: theoretical analysis and numerical simulations. J. Comput. Phys. 229, 760–787. https://doi.org/10.1016/j.jcp.2009.10.010.

Rosatti, G., Fraccarollo, L., 2006. A well-balanced approach for flows over mobile-bed with high sediment-transport. J. Comput. Phys. 220, 312–338. https://doi.org/10.1016/j.jcp.2006.05.012.

Rosatti, G., Zugliani, D., 2015. Modelling the transition between fixed and mobile bed conditions in two-phase free-surface flows: the composite Riemann Problem and its numerical solution. J. Comput. Phys. 285, 226–250. https://doi.org/10.1016/j.jcp.2015.01.011.

Rosatti, G., Zorzi, N., Zugliani, D., Piffer, S., Rizzi, A., 2018. A Web Service ecosystem for high-quality, cost-effective debris-flow hazard assessment. Environ. Model. Softw. 100, 33–47. https://doi.org/10.1016/j.envsoft.2017.11.017.

Salm, B., 1993. Flow, flow transition and runout distances of flowing avalanches. Ann. Glaciol. 18, 221–226. https://doi.org/10.3189/S0260305500011551.

Sampl, P., Zwinger, T., 2004. Avalanche simulation with SAMOS. Ann. Glaciol. 38, 393–398. https://doi.org/10.3189/172756404781814780.

Savage, S.B., Hutter, K., 1989. The motion of a finite mass of granular material down a rough incline. J. Fluid Mech. 199, 177–215. https://doi.org/10.1017/S0022112089000340.

Savage, S.B., Hutter, K., 1991. The dynamics of avalanches of granular materials from initiation to runout. Part I: Analysis. Acta Mech. 86, 201–223. https://doi.org/10.1007/bf01175958.

Sovilla, B., Burlando, P., Bartelt, P., 2006. Field experiments and numerical modeling of mass entrainment in snow avalanches. J. Geophys. Res. Earth Surf. 111, F03007 https://doi.org/10.1029/2005JF000391.

Toro, E.F., 2009. Riemann Solvers and Numerical Methods for Fluid Dynamics: A Practical Introduction. Springer, Third ed.. https://doi.org/10.1007/978-3-540-49834-6

Voellmy, A., 1955. Über die Zerstörungskraft von Lawinen. Schweizerische Bauzeitung 73, 159–162, 212–217; 246–249; 280–285. https://doi.org/10.5169/seals-61878.

Vreugdenhil, C.B., 1994. Numerical methods for shallow-water flow. Springer Netherlands. https://doi.org/10.1007/978-94-015-8354-1.

Zugliani, D., Rosatti, G., 2016. A new Osher Riemann solver for shallow water flow over fixed or mobile bed. In: Sustainable Hydraulics in the Era of Global Change - Proceedings of the 4th European Congress of the IAHR, Liege, Belgium, 27-29 July. CRC Press/Balkema, pp. 707–713.